

2011

## Quantitative Analysis of Dynamic Contrast-Enhanced Magnetic Resonance Breast Images: Optimization of the Time-to-Peak as a Diagnostic Indicator

Fang Liu

Follow this and additional works at: <https://ir.lib.uwo.ca/digitizedtheses>

---

### Recommended Citation

Liu, Fang, "Quantitative Analysis of Dynamic Contrast-Enhanced Magnetic Resonance Breast Images: Optimization of the Time-to-Peak as a Diagnostic Indicator" (2011). *Digitized Theses*. 3498.  
<https://ir.lib.uwo.ca/digitizedtheses/3498>

This Thesis is brought to you for free and open access by the Digitized Special Collections at Scholarship@Western. It has been accepted for inclusion in Digitized Theses by an authorized administrator of Scholarship@Western. For more information, please contact [wlsadmin@uwo.ca](mailto:wlsadmin@uwo.ca).

**Quantitative Analysis of Dynamic Contrast-Enhanced  
Magnetic Resonance Breast Images: Optimization of the  
Time-to-Peak as a Diagnostic Indicator**

(Spine Title: Time-to-Peak Analysis in Breast DCE-MRI)

(Thesis Format: Integrated Article)

by

**Fang Liu**

Graduate Program in Medical Biophysics

A thesis submitted in partial fulfillment  
of the requirements for the degree of

**Master of Science**

School of Graduate and Postdoctoral Studies

The University of Western Ontario

London, Ontario

March, 2011

© Fang Liu 2011

THE UNIVERSITY OF WESTERN ONTARIO  
SCHOOL OF GRADUATE AND POSTDOCTORAL STUDIES

**CERTIFICATE OF EXAMINATION**

Supervisor

\_\_\_\_\_  
Dr. Neil Gelman

Supervisory Committee

\_\_\_\_\_  
Dr. Giles Santyr

\_\_\_\_\_  
Dr. Eugene Wong

Examiners

\_\_\_\_\_  
Dr. Giles Santyr

\_\_\_\_\_  
Dr. Keith St. Lawrence

\_\_\_\_\_  
Dr. Giulio Muscedere

The thesis by

**Fang Liu**

entitled:

**Quantitative Analysis of Dynamic Contrast-Enhanced  
Magnetic Resonance Breast Images: Optimization of the  
Time-to-Peak as a Diagnostic Indicator**

is accepted in partial fulfillment of the requirements for the degree of

Master of Science

Date \_\_\_\_\_

\_\_\_\_\_  
Chair of the Thesis Examination Board

# ABSTRACT

Dynamic contrast-enhanced MRI (DCE-MRI) has been widely used in the diagnosis of breast cancer and as an aid in the management of this disease. Although DCE-MRI has a high sensitivity for the detection of malignant breast lesions, distinguishing malignant from benign lesions is more challenging for this method and may depend to some extent on how the images are analysed. Although clinical assessment of these images typically involves qualitative assessment by an expert, there is growing interest in the development of quantitative and automated methods to assist the expert assessment. This thesis involves the quantitative analysis of a particular empirical feature of the time evolution of the DCE-MRI signal known as the time-to-peak ( $T_{\text{peak}}$ ). In particular, this thesis investigates the feasibility of applying measures sensitive to  $T_{\text{peak}}$  heterogeneity as indicators for malignancy in breast DCE-MRI.

Breast lesions in this study were automatically segmented by K-means clustering. Voxel-by-voxel  $T_{\text{peak}}$  values were extracted using an empirical model. The  $p^{\text{th}}$  percentile values ( $p = 10, 20, \dots$ ) of the  $T_{\text{peak}}$  distribution within each lesion, as well as the fractional and absolute hot spot volumes were determined, where hot spot volume refers to the volume of tissue with  $T_{\text{peak}}$  less than a threshold value. Using the area under the receiver operating characteristic curve (AUC), these measures were tested as indicators for differentiating fibroadenomas from invasive lesions and from ductal carcinoma in situ, as well as for differentiating non-fibroadenoma benign lesions from these malignant lesions. For differentiating fibroadenomas from malignant lesions, low percentile values ( $p = 10$ ) provided high diagnostic performance. At the optimal threshold (3 min), the hot spot volume provided high diagnostic performance. However, non-fibroadenoma benign lesions were quite difficult to distinguish from malignant lesions. This thesis demonstrates that quantitative analysis of the  $T_{\text{peak}}$  distribution can be optimized for diagnostic performance providing indicators sensitive to intra-lesion  $T_{\text{peak}}$  heterogeneity.

***Keywords:*** breast cancer, dynamic contrast-enhanced MRI, lesion heterogeneity, time-to-peak distribution, lesion volume

# CO-AUTHORSHIP

The body of this thesis consists of one study (Chapter 2) that has been accepted for publication in a peer-reviewed journal (*Academic Radiology*). The title and authorship of this chapter is as follows:

## **Chapter 2:**

*Title:* Optimization of Time-to-peak Analysis for Differentiating Malignant and Benign Breast Lesions with Dynamic Contrast-Enhanced MRI

*Authorship:* F Liu (F.L.), A Kornecki (A.K.), O Shmuilovich (O.S.), and N Gelman (N.G.)

As the primary author of this manuscript, F Liu accomplished the following:

- a) converted and processed all dynamic contrast-enhanced magnetic resonance imaging (DCE-MRI) data acquired from the local MR scanner;
- b) designed and wrote all image processing software tools with Matlab. These tools accomplished several functions including automatic breast lesion segmentation, kinetic feature extraction after non-linear curve fitting, statistical analysis and diagnostic performance evaluation;
- c) assisted the radiologists (A.K. and O.S.) in utilizing my software tools for lesion delineation and identification;
- d) performed all DCE-MRI data analysis and statistical analysis;
- e) wrote the first draft of the manuscript, incorporated the revisions suggested by N.G. into subsequent drafts, and incorporated revisions suggested by all co-authors into the final draft.

In the memory of my grandmother Suqing Li

To my parents Wenjian Liu and Chutao Wang for their patience,  
understanding, support and love

# ACKNOWLEDGMENTS

I would like to express my greatest gratitude and recognition to my supervisor Neil Gelman, PhD who is the kindest and most knowledgeable scientist I have ever worked with. The successful completion of my thesis work is largely attributed to the invaluable discussions with Dr. Gelman and his intelligent suggestions and ideas that dramatically facilitated this work. His enthusiastic commitment, invaluable help and support ensured the accomplishment of this whole project, consequent manuscript, conference abstracts and of course this thesis.

The very important contributions of Anat Kornecki MD and Olga Shmuilovich MD, including patient selection, extracting pathological and diagnostic information, identifying lesions, etc., is greatly appreciated. I would also like to thank them for explaining important concepts in clinical breast cancer imaging. Their assistance was clearly indispensable for the progress of this project.

I also would like to acknowledge the members of my advisory committee Giles Santyr PhD and Eugene Wong PhD for their guiding ideas and constructive suggestions for the project, fruitful discussions and meetings towards the completion of my thesis.

I would also like to thank Ally Silavi for his kind suggestions regarding Matlab coding.

# TABLE OF CONTENTS

<i>TITLE PAGE</i>	I
<i>CERTIFICATE OF EXAMINATION</i>	II
<i>ABSTRACT</i>	III
<i>CO-AUTHORSHIP</i>	IV
<i>DEDICATION</i>	V
<i>ACKNOWLEDGMENTS</i>	VI
<i>TABLE OF CONTENTS</i>	VII
<i>LIST OF FIGURES</i>	X
<i>LIST OF TABLES</i>	XI
<i>LIST OF ABBREVIATIONS</i>	XII
<b>CHAPTER 1:</b>	
<i>Introduction</i>	
<b>1.1 Motivation.....</b>	<b>1</b>
<b>1.2 Breast Cancer .....</b>	<b>1</b>
<b>1.3 Diagnostic Imaging in Breast Cancer .....</b>	<b>3</b>
1.3.1 X-ray Mammography in Breast Cancer .....	4
1.3.2 Ultrasound in Breast Cancer .....	4
1.3.3 Magnetic Resonance Imaging in Breast Cancer .....	5
<b>1.4 Principles of Magnetic Resonance Imaging.....</b>	<b>6</b>
1.4.1 Magnetic Resonance (MR) Signal.....	6
1.4.2 3D Spoiled Gradient Echo Sequence.....	8
1.4.3 Dynamic Contrast-Enhanced MRI .....	10
<b>1.5 Analysis of Signal Kinetics in DCE-MR Images .....</b>	<b>12</b>
1.5.1 Overview of Empirical Kinetic Features .....	13
1.5.2 The Time-to-peak as an Empirical Kinetic Feature.....	14

1.6	Specific Techniques for Image Analysis in this Thesis.....	15
1.6.1	Lesion Segmentation.....	15
1.6.2	Curve Fitting with an Empirical Model.....	19
1.6.3	Histogram Analysis.....	21
1.7	Evaluation of Diagnostic Performance .....	23
1.8	Thesis Objectives .....	25
1.9	Thesis Outline .....	27
1.10	References.....	27

**CHAPTER 2:**

*Optimization of Time-to-peak Analysis for Differentiating Malignant and Benign Breast Lesions with Dynamic Contrast-Enhanced MRI*

2.1	Introduction.....	32
2.2	Materials and Methods .....	33
2.2.1	Patients and Lesions.....	33
2.2.2	Image Acquisition.....	35
2.2.3	Whole Lesion Image Analysis.....	36
2.2.4	Region of Interest Image Analysis.....	37
2.2.5	Receiver Operating Characteristic (ROC) Analysis .....	37
2.3	Results .....	38
2.4	Discussion .....	50
2.5	Appendix .....	55
2.6	References.....	56

**CHAPTER 3:**

*Summary and Future Work*

3.1	Summary of Findings .....	60
3.2	Future Work .....	62
3.3	Conclusions.....	63
3.4	References.....	64

<b><i>Appendix I:</i></b>	
<b><i>Ethics Approval for Breast Cancer Studies</i></b>	<b>65</b>
<b><i>Appendix II:</i></b>	
<b><i>Copyright Release</i></b>	<b>67</b>
<b><i>Appendix III:</i></b>	
<b><i>Curriculum Vitae</i></b>	<b>68</b>

# LIST OF FIGURES

<b>Figure 1-1.</b> Diffusion of a contrast agent into tissue. ....	11
<b>Figure 1-2.</b> One example of lesion segmentation using the K-means clustering method from the data used for Chapter 2. ....	19
<b>Figure 1-3.</b> Curve fitting with the empirical model proposed by Gal et al. ....	21
<b>Figure 1-4.</b> $T_{\text{peak}}$ distribution demonstrates the intra-lesion heterogeneity of breast lesions.....	22
<b>Figure 1-5.</b> Hypothetical ROC curves for two measures. ....	25
<b>Figure 2-1.</b> Median percentile $T_{\text{peak}}$ values and ROI-based $T_{\text{peak}}$ values (a) as well as AUC values corresponding to percentile $T_{\text{peak}}$ values (b). ....	40
<b>Figure 2-2.</b> Median fractional hot spot volumes (a) and corresponding AUC values (b). ....	42
<b>Figure 2-3.</b> Median absolute hot spot volumes (a) and corresponding AUC values (b). ....	44
<b>Figure 2-4.</b> Receiver operating characteristic (ROC) curves for differentiating fibroadenoma versus invasive lesions and fibroadenoma versus DCIS using ROI-based analysis and absolute hot spot volume at a $T_{\text{peak}}$ threshold of 3 min. ....	46
<b>Figure 2-5.</b> Relationship between absolute hot spot volume ( $T_{\text{peak}}$ threshold of 3 min) and lesion volume for fibroadenomas (empty up triangles), non-fibroadenoma benign lesions (empty squares), DCIS (filled down triangles) and invasive lesions (filled circles). ....	48
<b>Figure 2-6.</b> Absolute hot spot volumes at a $T_{\text{peak}}$ threshold of 3 min for lesions within each histopathological type. ....	49
<b>Figure 2-7.</b> Relationship of $T_{\text{peak}}$ and $k_{\text{ep}}$ obtained by numerical simulation. ....	56

## LIST OF TABLES

<b>Table 1-1.</b> A $2 \times 2$ contingency table for comparing the outcomes from a gold standard and a measure to be tested in binary classification. ....	23
<b>Table 2-1.</b> Histopathological diagnosis for the 136 breast lesions. ....	35
<b>Table 2-2.</b> AUC values for 5 measures in differentiating 4 groups of breast lesions. ....	47
<b>Table 2-3.</b> Linear regression analysis for absolute hot spot volume at a threshold of 3 min versus lesion volume. ....	49

## LIST OF ABBREVIATIONS

$\rho$	proton density
$\theta$	flip angle in radians
2D	two-dimensional
3D	three-dimensional
3TP	three-time-points
$A$	relaxivity
AUC	the area under the ROC curve
$B_0$	static magnetic field
$B_1$	radio frequency magnetic field
$C_{\text{Gd-DTPA}}$	concentration of Gd-DTPA
CT	X-ray computed tomography
DCIS	ductal carcinoma in situ
DCE	dynamic contrast-enhanced
DCE-MRI	dynamic contrast-enhanced MRI
FA	flip angle
$G$	proportionality coefficient
Gd-DTPA	gadopentetate dimeglumine
IDC	invasive ductal carcinoma
ILC	invasive lobular carcinoma
$k_{\text{ep}}$	rate constant
$K_{\text{trans}}$	endothelial transfer constant
LCIS	lobular carcinoma in situ
MR	magnetic resonance
MRI	magnetic resonance imaging
MSE	mean square errors
$PE$	percentage enhancement ratio
rf	radio frequency
$R_1$	longitudinal relaxation rate
$R_{10}$	longitudinal relaxation rate without contrast agent
$R^2$	correlation coefficients
ROC	receiver operating characteristic
ROI	region-of-interest
$S$	MR signal intensity
$SER$	signal enhancement ratio
SNR	signal to noise ratio
SPAIR	spectral adiabatic inversion recovery
SPGR	spoiled gradient echo
T	Tesla

$T_1$	longitudinal relaxation time
$T_2$	transverse relaxation time
$T_2^*$	effective transverse relaxation time
$TE$	time of echo
$T_{\text{peak}}$	time-to-peak
$TR$	time of repetition
US	ultrasound
VIBE	volume interpolated breath hold imaging
$x$	$x$ Cartesian coordinate
$y$	$y$ Cartesian coordinate
$z$	$z$ Cartesian coordinate

# Introduction

## 1.1 Motivation

Breast cancer is the most common cancer and the second most common cause of cancer deaths among Canadian women. In 2010, an estimated 23,200 Canadian women will be diagnosed with breast cancer and 5,300 women will die from this disease (1, 2). The number of breast cancer deaths has remained unchanged since 2009 (2). Based on the breast cancer incidence estimates, one in nine Canadian women is expected to develop breast cancer during their lifetime (by age 90) and one in 28 will die of this disorder.

The rate of detection of breast cancer has gradually increased since the early 1980s, largely due to the increased use of mammographic screening (3). However, the death rate from breast cancer declined in every age group after the mid 1980s and even more after the mid 1990s. This has mainly been attributed to both advances in treatments and improvements in breast cancer screening (2, 4). A large number of studies (3-11) have suggested that the decrease in breast cancer related mortality and morbidity that occurred in recent decades is due to early detection and accurate diagnosis. Imaging techniques including magnetic resonance imaging provide an important contribution to early breast cancer detection and diagnosis.

## 1.2 Breast Cancer

Breast cancer usually originates from the ducts and lobules (milk producing unit) of the breast tissue, but very rarely from the stroma (connective supporting tissue). Malignant breast tumors can be classified according to the site of origin and the status of invasiveness. Non-invasive breast cancer refers to cancer that is confined within the milk ducts and/or lobules of the breast. Although these cancers are considered to be non-invasive, they can progress to invasive cancers. More specifically, Ductal carcinoma in situ (DCIS) is a non-invasive cancer which is located within ducts and has not infiltrated

through the duct walls. Lobular carcinoma in situ (LCIS) on the other hand, corresponds to cancer that originates in the lobules and remains at that site at the time of detection. Invasive breast cancer refers to cancer in which cancer cells have penetrated through the walls of the ducts and/or lobules into the surrounding normal breast tissue. Invasive breast cancer usually has a worse prognosis than non-invasive cancer because the cancer cells can further penetrate the wall of blood and/or lymphatic vessels and spread through the bloodstream or lymphatic system to distant organs leading to the development of metastatic cancers. Invasive cancer originating from the ducts, known as invasive ductal carcinoma (IDC), is the most common type of invasive breast cancer. Invasive lobular carcinoma (ILC) is invasive cancer originating from lobules.

Benign breast tumors consist of a heterogeneous group of tumors that may show a wide range of symptoms. Differing from malignant breast tumors, benign breast tumors do not invade other tissue or metastasize to other organs. These tumors do not normally lead to mortality but may cause pain or discomfort for patients. Also the presence of certain benign tumors may be associated with an increased risk of breast cancer (12, 13). Various types of benign breast tumors occur. The types that are included in the study presented in Chapter 2 are fibroadenomas, fibrocystic changes, apocrine metaplasia, radial scars, intraductal papillomas, complex papillary lesions, fibrosis and fat necrosis. These tumors can also be categorized based on the sites where they occur. Benign lesions that originate from lobules include fibroadenomas and apocrine metaplasia; those that originate from ducts include radial scars, intraductal papillomas, and complex papillary lesions; and those that originate from other breast tissue (e.g., stroma or adipose tissue) include fibrosis and fat necrosis. Fibroadenomas are the most common benign solid tumors that arise in the lobules. They are composed of fibrous stromal tissue and characterized by proliferation of the stroma, which leads to distortion of ductal system within the breast. Although the word “scar” occurs in “radial scar” this benign lesion is not scar tissue related to trauma or surgery. Papillary lesions of the breast include a broad range of lesions which are characterized by a fibrovascular core covered by epithelial fronds (protrusions) composed of two layers of epithelial cells. Intraductal papillomas are papillary lesions within a dilated duct or ducts. Fibrosis is characterized by the

proliferation of stroma which results in a localized area of fibrous tissue associated with hypoplasia of ducts and lobules (14). (Hypoplasia refers to a decrease in the number of cells relative that in the corresponding normal tissue.) Fat necrosis of the breast results from a benign inflammatory process of adipose tissue related to breast trauma or surgery. The fat necrosis lesion consists of oily debris, fibrous connective tissue, foamy macrophages and giant cells. Fibrocystic changes represent the most frequent benign breast disorders and include a large range of breast tissue changes. They can arise from the ducts (e.g., ductal hyperplasia) or from the lobules (e.g., adenosis, sclerosing adenosis and apocrine metaplasia). Apocrine metaplasia, one type of fibrocystic changes, refers to the presence of breast tissue epithelial cells which resemble the cells of apocrine glands.

During the development of a tumor, the formation of networks of new microvessels known as neoangiogenesis plays an important role for supplying nutrients and oxygen for tumor growth. The angiogenic factors released by tumor cells interact with endothelial cells in the neighbouring vessels and stimulate the generation of new microvessels, resulting in high tumor microvessel density and an increase in perfusion (15). In addition, the pores in the basement membrane of the newly formed vessels are more open than in normal vessels, resulting in high permeability of these vessels to large molecules in the blood plasma. Blood perfusion and microvessel permeability are therefore considered physiological correlates to the changes in tumor vessels that are associated with tumor neoangiogenesis. Neoangiogenesis can occur in both malignant breast tumors (i.e., breast cancer) where the growth of tumor cells appears to be invasive, and benign breast tumors, which are considered non-cancerous and non-invasive (16).

### **1.3 Diagnostic Imaging in Breast Cancer**

Early and accurate diagnosis of breast cancer has been positively linked to a decrease in the mortality and morbidity of the illness. Imaging techniques involved in clinical breast cancer diagnosis normally include X-ray mammography, ultrasound, and magnetic resonance imaging. Other imaging techniques such as positron emission tomography and scintigraphy are also used as complementary tools in selected cases (11).

### **1.3.1 X-ray Mammography in Breast Cancer**

X-ray mammography is the conventional technique for breast screening in clinical practice. In X-ray mammography, the breast is compressed using mammography plates in order to even out the thickness of the breast tissue. The compressed breast is then exposed to a low dose of X-rays, from which a two-dimensional (2D) diagnostic image is formed either on X-ray film or solid-state detectors that convert X-rays into electrical signals. Screening mammography has been shown to be an effective method for detecting breast cancer. Studies (5, 17) have indicated that women aged 50 to 69 years who received mammography screening had a lower breast cancer mortality rate by 20% to 35% at a 14 year follow-up compared to those who were not screened. For women aged 40 to 49 years the reduction in mortality was slightly less. Although X-ray mammography is used routinely for breast cancer screening, some limitations exist. The limited sensitivity of X-ray mammography (i.e., high 'false negative' rate) is largely due to the presence of dense breast tissue (especially for younger women) which may obscure the cancer as well as the overlap of cancerous tissue and normal breast tissue in a two dimensional image (5, 18). From the results of seven population-based community screening programs in the United States on 463,372 screening mammograms from 1996 to 1998, the sensitivity ranged from 0.63 in women with extremely dense breasts to 0.87 in women with almost entirely fatty breast. Also the sensitivity ranged from 0.69 in women aged 40 through 44 years to 0.83 in women aged 80 through 89 years (18). The use of ionizing radiation is also a disadvantage of X-ray mammography.

### **1.3.2 Ultrasound in Breast Cancer**

Ultrasound (US) uses high frequency sound waves to detect breast tumors. Compared to X-ray mammography, US has the advantage of not involving ionizing radiation. Compared to MRI, ultrasound has the advantage of being more widely available, less expensive and without contrast agent induced complications (6). In addition, US has the ability to provide real-time image guidance for needle core biopsy procedures (7). Breast abnormalities identified on mammography or other image

modalities can be classified as solid or fluid filled using US (6, 7). However, the drawbacks of US include the limited ability for evaluating microcalcifications and higher false positive rates than X-ray mammography (6, 7, 19-21). Also since the US procedure is to a large extent under manual control, the diagnostic performance may to some extent vary between ultrasonographers. A recent study found that including US with mammography for screening yielded a higher detection rate for high-risk women and women with dense breasts than using mammography alone, but substantially increased the number of false positives (22).

### **1.3.3 Magnetic Resonance Imaging in Breast Cancer**

Magnetic resonance imaging (MRI) is frequently utilized in the diagnosis of breast cancer and has been also used for other applications including breast cancer screening, imaging guided breast biopsy, monitoring cancer response to chemotherapy and/or radiation therapy and for surgical planning (8, 11). One of the most commonly used breast MRI methods is dynamic contrast-enhanced MRI (DCE-MRI). This method involves the intravenous injection of a contrast agent and the acquisition of magnetic resonance images over several minutes following the injection allowing the observation of changes in the magnetic resonance (MR) signal as a function of time. Numerous studies have shown the high diagnostic sensitivity of DCE-MRI for detecting malignant breast tumors. However, the specificity varies and remains a challenge. Peters et al. (23) performed a meta-analysis study to investigate the diagnostic performance of contrast-enhanced MRI for differentiating malignant from benign breast lesions. In their study, the diagnostic sensitivity and specificity values of 44 eligible previous studies from 1985 to 2005 were analyzed. The average sensitivity was found to be 0.90 with 95% confidence interval of 0.88 to 0.92, and the average specificity was 0.72 with 95% confidence interval of 0.67 to 0.77. This study demonstrated that diagnostic specificity remains a challenge for the application of DCE-MRI for breast cancer diagnosis. The current consensus is MRI is excellent for detecting multifocal/multicentric breast tumors and determining tumor extent (11, 24-26).

## **1.4 Principles of Magnetic Resonance Imaging**

Magnetic Resonance Imaging is an imaging technique that can provide strong contrast between soft tissues and hence it is often employed for visualization of anatomical structures within soft tissue. This imaging modality is now widely used in neurological, cardiovascular and oncological applications. MRI is a relatively new technology compared with ionizing radiation based techniques such as X-ray image and X-ray computed tomography (CT). The first MR image was published in 1973 and the first studies of humans were published in 1977. MR images are constructed from the nuclear magnetic resonance signals from water (and fat) protons in tissue.

### **1.4.1 Magnetic Resonance (MR) Signal**

The main magnet of the MRI system produces a powerful static magnetic field (usually called the  $B_0$  field) which, for modern clinical MRI systems, is typically 1.5 Tesla or greater. When a proton containing material such as tissue is placed within this large magnetic field, there is a slight tendency for proton magnetic moments to align along the direction of the magnetic field, thus forming a net magnetization associated with these protons. This magnetization, known as the thermal equilibrium magnetization, only has a component along the direction of the static magnetic field, defined as the  $z$ -direction (i.e., the  $x$ - and  $y$ - components equal to zero). The magnetization associated with the protons of water (and fat) will contribute to the MRI signal. In order to generate this signal, a radio frequency (rf) transmitter (or coil) will be briefly turned on to produce a radio frequency magnetic field (called the  $B_1$  field) at, or close to, the frequency at which the proton magnetic moments can absorb energy, allowing the magnetization to be manipulated. This frequency, known as the Larmor frequency, depends on field strength and nuclear species (in this case protons). While the  $B_1$  magnetic field is on, the proton magnetization rotates away from the direction of the static magnetic field through a particular angle known as the flip angle (FA). The amplitude and duration of the radio frequency magnetic field controls the flip angle. Once the magnetization is no longer parallel to the static magnetic field it starts to precess at the Larmor frequency about the

static magnetic field direction. After the transmitter is turned off, the magnetization continues to precess at the Larmor frequency. During this process, the signal produced by the precession of the magnetization is detected by a radio frequency receiver coil. The evolution of the magnetization, and hence the signal generated, also depends on two MRI parameters known as the  $T_1$  and  $T_2$  relaxation times.  $T_1$  is the time constant describing the exponential re-growth of longitudinal magnetization (z-component) towards its thermal equilibrium value. Similarly,  $T_2$  is defined to characterize the decay of the transverse magnetization (combination of x- and y-components) to their thermal equilibrium values (both equal to zero).

The creation of an image using MR signals requires the application of magnetic field gradients to spatially encode information regarding the position where the signal components arise from. There are three principle methods of spatial encoding known as frequency encoding, phase encoding and slice selection. Typical imaging acquisitions use either all three (one for each direction in space) or only the first two. Both frequency encoding and phase encoding use the principle that the magnetization precesses at a frequency that is dependent on the strength of the magnetic field at the position in space where this magnetization is located. Thus, when the magnetic field gradient is applied, the magnetization at different positions along the gradient direction accumulate different amounts of phase during a given elapsed time. In the case of phase encoding, the magnetic field gradient is switched on shortly after the rf excitation pulse and prior to the signal readout, and then turned off during signal acquisition. This encodes position-dependent phase into the signal. The strength of phase encoding gradient field changes by a certain increment with each acquired signal. The frequency encoding gradient, on the other hand, is switched on just prior to the signal acquisition and remains on during the signal acquisition, encoding position-dependent frequency into the signal. The signal amplitudes acquired as a function of phase encoding step and frequency encoding time point are used to fill in data points in a space known as k-space. The spatial reconstruction of MR image can be obtained by calculating the Fourier Transform of the k-space data. Finally, slice selection involves the use of a designed slice selective rf pulse having specific frequency bandwidth. When slice selection gradient field is applied, only

proton magnetic moments within a particular slice corresponding to the frequency bandwidth range centered at the Larmor frequency can absorb energy, and thus be manipulated.

In breast MRI, the image must cover the whole breast. There are two different approaches for obtaining such a three-dimensional (3D) block of image data. One method, known as multi-slice imaging involves acquiring a series of 2D slices covering the whole breast volume. With multi-slice imaging, spatial encoding is accomplished by frequency encoding in one direction, phase encoding in the second direction and slice-selection in the third direction. Although multi-slice imaging does acquire images over a 3D volume it is not generally referred to as 3D imaging in the MRI literature. The second method, which is referred to as 3D MRI, is performed by replacing slice selection by phase encoding, i.e., two directions are spatially encoded by phase encoding. With 3D MRI, all three directions are spatially encoded by Fourier-based methods (frequency or phase encoding).

For breast imaging, 3D MRI has several advantages over multi-slice MRI. First, the 3D acquisition typically results in a higher signal to noise ratio (SNR) than that of multi-slice MRI. Therefore, thinner slices with reasonable SNR can be obtained with the 3D MRI method and, in particular, the image voxels can be isotropic, i.e., have the same size in each dimension. Second, in multi-slice imaging it is often necessary to leave a small gap (typically approximately 30% of the slice width) between slices to prevent the signal from neighbouring slices from interfering with each other. Although this problem can be avoided by acquiring two sets of interleaved slices, this requires doubling the imaging time. Thirdly, multi-slice imaging is limited by imperfect slice selection profiles and, hence, the flip angle will vary across each slice.

### **1.4.2 3D Spoiled Gradient Echo Sequence**

In clinical practice, the 3D low flip angle spoiled gradient echo (SPGR) sequence is widely used for collecting breast images. This sequence consists of a series of rf pulses

applied to the magnetization. Between each rf pulse, the longitudinal magnetization does not recover fully to its thermal equilibrium value. The SPGR sequence employs a technique known as rf spoiling that affects the signal in such a way as to approximately emulate a signal in which the transverse magnetization just prior to each rf pulse has been destroyed. After a sufficient number of cycles that depend on the FA and repetition time of rf pulses ( $TR$ ), this process reaches a steady state where the magnetization has an identical behaviour during each rf cycle. When the magnetization has achieved steady state, the signal equation for the spoiled gradient echo sequence is given as:

$$S = G * \rho * e^{-\frac{TE}{T_2^*}} * \sin(\theta) * \frac{1 - e^{-\frac{TR}{T_1}}}{1 - \cos(\theta) * e^{-\frac{TR}{T_1}}},$$

where  $S$  is the MR signal at steady state,  $G$  is a proportionality coefficient depending on the receiver gain,  $\rho$  is the proton density,  $\theta$  is the flip angle in radians,  $TE$  is the Time of Echo,  $T_2^*$  is a time constant describing the signal decay as a function of  $TE$ . (This decay is due to both transverse relaxation and intra-voxel dephasing of the magnetization caused by various factors, e.g., external magnetic field inhomogeneity.) Under the condition of short  $TE$ ,  $TE/T_2^*$  can be quite small, in which case the MR signal is largely dependent on the longitudinal relaxation time constant  $T_1$ .

The data analyzed for this thesis (detailed in Chapter 2), had been acquired (clinically) using the 3D spoiled gradient echo sequence specifically known as volume interpolated breath hold imaging (VIBE). This sequence included fat suppression using a technique known as Spectral Adiabatic Inversion Recovery (SPAIR), which uses a spectrally selective adiabatic pulse to null the longitudinal magnetization from fat, by first inverting this magnetization and then acquiring the most “important” signals after a delay time set to allow this magnetization to reach zero. In the VIBE sequence, this inversion pulse is applied several times during the 3D acquisition. In our implementation, one inversion was applied prior to a group of 80 signals (80 k-space lines) and the delay had been set to null the fat magnetization for the signals within that group which were closest

to the k-space center. For the images acquired, the frequency encoding direction was posterior-anterior to avoid cardiac motion related ghosting from degrading the image within the breast regions. Also, the sequence employed a slab-selective excitation to eliminate any possible interfering image signal from superior or inferior to the breast tissue (i.e., due to aliasing in the superior inferior phase encode direction).

### **1.4.3 Dynamic Contrast-Enhanced MRI**

For dynamic contrast-enhanced MRI, a contrast agent is injected intravenously and its uptake by the breast tissue is tracked with repeated  $T_1$ -weighted imaging, typically using 3D SPGR. In a clinical setting, one 3D image is usually acquired within approximately one min, and there is no delay between successive acquisitions. Thus, the typical time resolution is approximately one min. The MRI signal changes over time reflect changes in contrast agent tissue concentration, since the contrast agent shortens the  $T_1$  relaxation time of surrounding water protons. Due to the development of abnormal microvasculature (neovascularization, as described in section 1.2) which is very “leaky” to the contrast agent, signal increase, known as enhancement, occurs within breast tumors. The enhancement changes as a function of time after the contrast agent injection. The contrast agent, which leaks out of the capillaries temporarily resides in the extravascular extracellular spaces, but does not enter the intracellular spaces (see Figure 1-1).

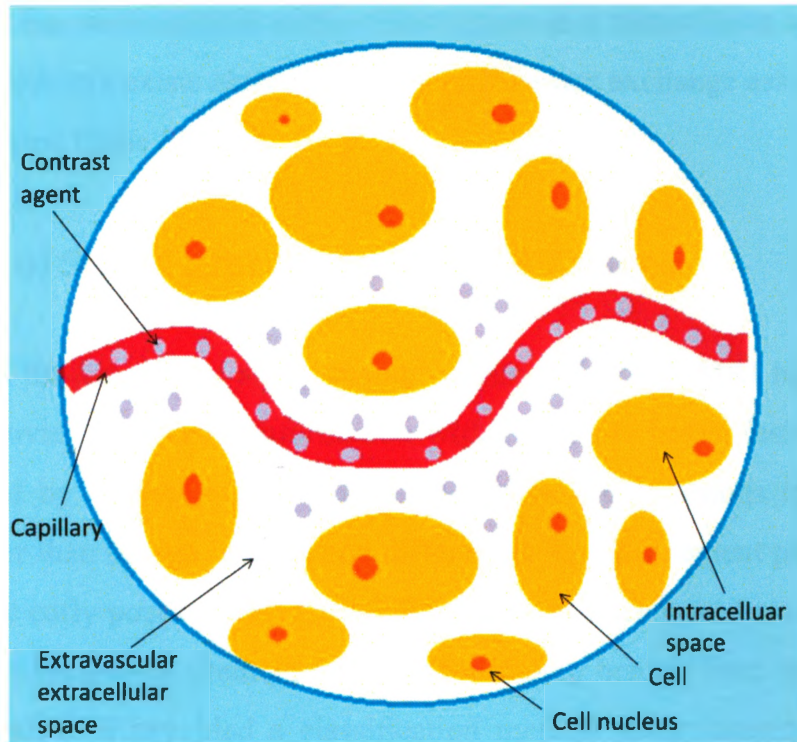


**Figure 1-1.** Diffusion of a contrast agent into tissue. The contrast agent is distributed in vascular plasma and extravascular extracellular space.

A contrast agent, which is widely used in breast DCE-MRI, is gadopentetate dimeglumine (Gd-DTPA). This agent is a paramagnetic complex containing a gadolinium ion with a chelating agent, diethylenetriamine penta-acetic acid. The dipole-dipole interaction between the unpaired electrons of the paramagnetic ions and the protons of the water shortens the  $T_1$  relaxation time of the protons, leading to a signal increase in  $T_1$  weighted images. The expected relaxation rate  $R_1$  ( $1/T_1$ ) in the presence of contrast agent has a linear relationship with the concentration of Gd-DTPA as given below:

$$R_1 = R_{10} + A * C_{\text{Gd-DTPA}} ,$$

where  $R_{10}$  is the longitudinal relaxation rate of water protons within the tissue in the absence of Gd-DTPA,  $C_{\text{Gd-DTPA}}$  is the concentration of Gd-DTPA, and  $A$  is the relaxivity. The application of this equation to the average signal from a given voxel assumes that there is fast exchange between different tissue compartments, in particular, the largest

spaces which are the extravascular extracellular space and intracellular spaces (27, 28). However, the debate still exists about the validity of the fast exchange assumption in both normal and abnormal tissue (29-32).

## **1.5 Analysis of Signal Kinetics in DCE-MR Images**

Analysis of the kinetics of signal evolution curves in DCE-MRI has been utilized extensively to provide diagnostic information with respect to breast lesion malignancy. As first described by Kaiser & Zeitler (33), malignant breast lesions tend to enhance faster and stronger than benign lesions, and differences in enhancement patterns are most pronounced in the early post-contrast period. Numerous studies have focused on utilizing kinetic features as diagnostic predictors for differentiating benign from malignant breast lesions. Kuhl et al. (34) provided a classification method using three types of kinetic curves, including the persistent or steady enhancement (type I), plateau (type II) and washout curves (type III). Using this classification they were able to distinguish benign from malignant tumors with a sensitivity of 91% and a specificity of 83% (34). Furman-Haran and Degani (35-37) produced a color-coded parametric map using the contrast enhancement patterns obtained using signals acquired at only three-time-points (3TP) following contrast injection. The wash-in phase defined by the signal intensity difference in the first two time points was coded by color intensity, and the wash-out phase as the change of enhancement between the last two time points was coded by color hue. Hauth et al. (38) compared the 3TP results with the results of region-of-interest (ROI) method for diagnosis of breast lesions in the dataset of 40 women. The 3TP method had the advantage of displaying the heterogeneity of the contrast enhancement pattern observed in malignant lesions and foregoing time-consuming and subjective manual ROI placement.

Quantitative methods for analyzing signal kinetics include both empirical methods and pharmacokinetic models. The latter describe the underlying physiology of contrast agent exchange between vascular plasma and extravascular extracellular space. However, these models may be challenging to apply for clinical imaging, due to the requirement for

measurements of the arterial input function and the native  $T_1$  value before contrast agent injection. In addition, the high temporal resolution required by these models may be difficult to obtain along with high spatial resolution and breast coverage required for clinical imaging. In contrast to pharmacokinetic parameters, quantitative empirical kinetic features may be more compatible with these practical requirements of clinical DCE-MRI.

### 1.5.1 Overview of Empirical Kinetic Features

Several empirical descriptive features have been introduced to describe DCE-MRI curve patterns. These include features characterizing signal enhancement at the early stage (wash-in phase) such as percentage enhancement ratio ( $PE$ ) (33) and uptake rate (39), as well as those describing signal decay (wash-out phase) such as signal enhancement ratio ( $SER$ ) (40) and washout rate (39). The  $PE$ , for example, is simply the enhancement of a given early post-contrast image signal ( $S_1$ ) relative to that of the pre-contrast image signal ( $S_0$ ), i.e.,  $PE = (S_1 - S_0)/S_0$ . In addition to these two signals, the  $SER$  also utilizes the signal ( $S_2$ ) at second post-contrast time point to describe the degree of washout ( $SER = (S_1 - S_0)/(S_2 - S_0)$ ). One limitation of these empirical features is that their values may be sensitive to the time points chosen by the user. In addition, since the values of these empirical features are calculated directly from signal intensity values, they are also dependent on imaging timing parameters (e.g.,  $TE$ ,  $TR$  and  $FA$ ), making comparisons between studies with different protocols difficult.

The empirical feature, which is the focus of this thesis, is known as the time-to-peak ( $T_{\text{peak}}$ ) (39, 41). It is defined as the time duration from the contrast agent injection to the maximal MR signal for a given voxel. One advantage of the  $T_{\text{peak}}$  is that at least in theory it should be independent of imaging timing parameters as the highest MR signal is expected to occur at the time at which the shortest  $T_1$  for a given voxel occurs. Also  $T_{\text{peak}}$  is a fundamental parameter describing the signal evolution and does not require the choice of specific time points.

## 1.5.2 The Time-to-peak as an Empirical Kinetic Feature

A few reports have investigated  $T_{\text{peak}}$  as a diagnostic indicator of malignancy. Ikeda et al. (39) identified useful features for differentiating malignant and benign breast lesions using logistic regression analysis. Two of the kinetic features, washout ratio and  $T_{\text{peak}}$ , were found to be the most reliable indicators for lesion malignancy. The resulting logistic regression model incorporating washout ratio and  $T_{\text{peak}}$  yielded a diagnostic accuracy of 91%. In a study by Szabo et al. (41) an assessment and comparison of the values of kinetic and morphological features in differentiating malignant from benign breast lesions were performed. Their results from 79 lesions indicated that  $T_{\text{peak}}$  was the most independent kinetic feature for distinguishing benign versus malignant lesions. Most recently, Chen et al. (42, 43) proposed an automatic fuzzy C-means clustering algorithm for breast lesion segmentation and lesion sub-region classification. Four kinetic features including maximum contrast enhancement,  $T_{\text{peak}}$ , uptake rate and washout rate were extracted from characteristic curves of the lesion. The results indicated significant differences between benign and malignant lesions only for  $T_{\text{peak}}$ .

Two of the previous reports discussed above (39, 41) in which  $T_{\text{peak}}$  was investigated as a diagnostic indicator were based on analysing signals from manually determined regions of interest (ROI). That is the  $T_{\text{peak}}$  values were determined from the average curve across all the voxels within the ROI. Since the position and size of the ROI selected was determined manually, one would expect that the values obtained might be sensitive to the individual preference and experience of the observer. Mussurakis et. al. (44-46) and Liney et. al. (47) in their studies demonstrated that the inter- and intra-observer variation caused by manual ROI selection can lead to varying diagnostic performance in breast DCE-MRI analysis.

This thesis will present a whole lesion voxel-by-voxel analysis of  $T_{\text{peak}}$ . Measures of the  $T_{\text{peak}}$  from the whole lesions should be free of the inter- and intra-observer variation problem. With this analysis, individual  $T_{\text{peak}}$  values are extracted for each voxel within the lesion and statistics about the  $T_{\text{peak}}$  distribution and other measures related to the intra-

lesion variation of  $T_{\text{peak}}$  values are analyzed. Other primary advantages of voxel-by-voxel analysis include the ability to investigate lesion heterogeneity. Previous reports using other DCE-MRI measures have demonstrated that intra-tumor heterogeneity can serve as indicators in the diagnosis of breast tumors (48-51).

The benign breast lesions analyzed in the previous studies involving  $T_{\text{peak}}$  were mixtures of different histopathological types. In general very few reports have assessed the specific challenges of differentiating different types of benign lesions from malignant lesions. The analysis presented in Chapter 2 will also extend previous work by considering lesion sub-types in the context of classifying malignant from benign lesions.

## **1.6 Specific Techniques for Image Analysis in this Thesis**

The development of computer-assisted techniques for automatic processing of image data should help improve the diagnostic performance and reproducibility of breast DCE-MR image analysis. Such a system can take advantage of powerful computer calculations for segmenting suspicious tissue areas and extracting features for lesion classification analysis. Several studies (24, 25, 52) have reported improvements in diagnostic specificity obtained with computer-assisted methods. Below is an introduction to the computer-assisted image processing techniques used in this thesis for breast lesion segmentation, including kinetic feature ( $T_{\text{peak}}$ ) extraction and histogram analysis.

### **1.6.1 Lesion Segmentation**

Lesion segmentation refers to the procedure for delineating suspicious tissue areas within medical images. This can be performed manually (i.e., by drawing a region of interest) or with automated (or semi-automated) computer-assisted methods. Most recently, Lee et al. (53) proposed a K-means clustering-based automatic segmentation method for analyzing breast DCE-MR images.

K-means clustering is a classification technique used in the pattern recognition field. One advantage of K-means clustering is that it can be applied to multi-dimensional

data where each data point can be represented by a point in a  $d$ -dimensional space (i.e., each data point has  $d$  components). Before describing how K-means clustering is applied to segmentation, its general principles will be outlined. The purpose of K-means clustering is to separate one dataset with multiple data points into  $k$  clusters such as to minimize the intra-cluster variation and maximize the inter-cluster variation. More specifically, suppose one dataset  $X$  has  $N$  data points, each of which is represented by  $x_i$  ( $i = 1, 2, \dots, N$ ), and the centroid of each cluster is represented by  $v_j$  ( $j = 1, 2, \dots, k$ ). Then the goal of the clustering algorithm is to iteratively try to minimize the least squares within-group square error function  $F$  :

$$F = \sum_{j=1}^k \sum_{i=1}^N u_{ij} \|x_i - v_j\|^2 ,$$

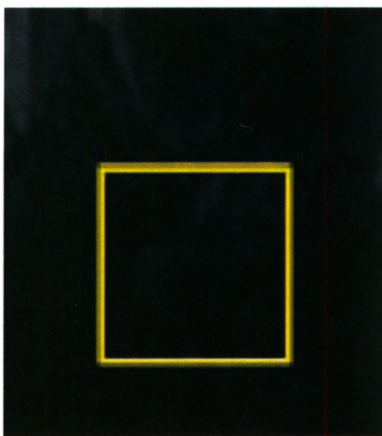
where  $\| \cdot \|$  denotes the Euclidean distance and  $u_{ij}$  is the membership value that has a value of 1 if  $x_i$  belongs to  $j^{\text{th}}$  cluster, or a value of 0 if  $x_i$  doesn't. The centroid ( $v_j$ ) for  $j^{\text{th}}$  cluster is the average value of the data points in this cluster, then given as:

$$v_j = \frac{\sum_{i=1}^N u_{ij} \cdot x_i}{\sum_{i=1}^N u_{ij}}, \quad j = 1, 2, \dots, k .$$

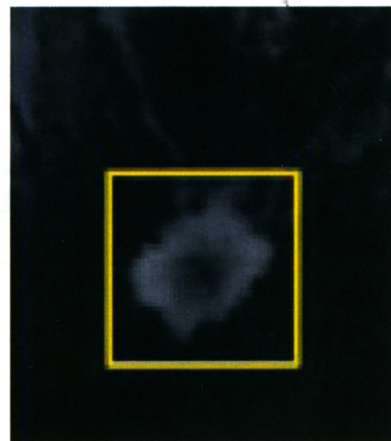
In the application of K-means clustering for the segmentation of DCE-MRI data the following correspondence can be made to the generalized data discussed above. For each voxel (i.e.,  $x_i$ ,  $i = 1, 2, \dots, N$ ) in the image there is a series of MR signals, one from each of the post-contrast images (seven images in our implementation). This series of signals will be referred to in the paragraph below as a "signal curve" even though it is a set of seven discrete signal values. The  $N$  voxels correspond to  $N$  data points (i.e.,  $x_i$ ,  $i = 1, 2, \dots, N$ ) and the data points exist within a  $d$ -dimensional space, where  $d$  is the number of post contrast images ( $d = 7$  in our implementation). The goal is to separate these  $N$   $d$ -dimensional data points (voxel signals) into  $k$  clusters. In the present, case  $k = 2$  was chosen, where the two clusters correspond to normal and abnormal tissue.

An example of breast lesion segmentation using K-means clustering as implemented for the analysis presented in Chapter 2 is shown in Figure 1-2. Prior to performing the K-means clustering a radiologist was required to draw a 3D rectangular box enclosing the suspicious breast lesion. The yellow box in Figure 1-2 is a 2D slice from this box. Then the coordinates of the box were passed to the lesion segmentation tool incorporating the K-means clustering algorithm. Using this segmentation tool the tissue within the box was classified into two clusters (i.e.,  $k = 2$ ), one representing “normal tissue” and the other abnormal tissue. Further details about the K-means clustering procedure applied in Chapter 2 are given as follows:

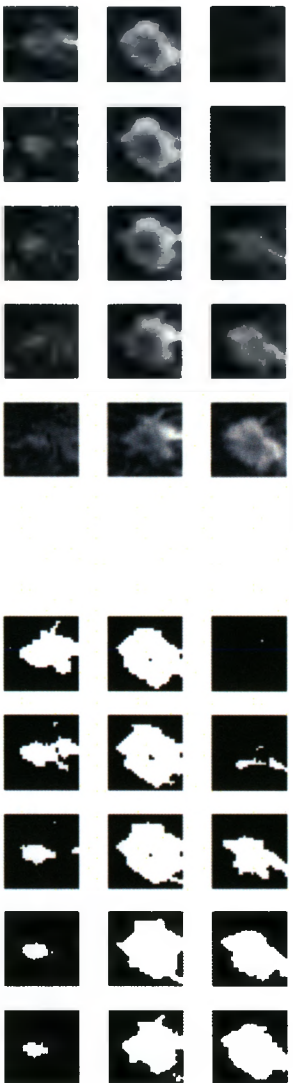
i) The pre-contrast image was subtracted from seven post-contrast images. ii) For each of the two clusters ( $j = 1, 2$ ), one signal curve was randomly chosen from all signal curves as the initial guess for  $v_j$ . iii) Each signal curve ( $x_i, i = 1, 2, \dots, N$ ) was assigned to the cluster with the centroid ( $v_j$ ) that was closest to it, i.e., based on the Euclidean distance in the  $d$ -dimensional space. iv) After the assignment of all the signal curves into two clusters, the centroids of these two clusters were recalculated to find new cluster centroids using above equation. v) Steps iii) and iv) were repeated until the algorithm converges near a minimal value of least squares within-group error function,  $F$ .



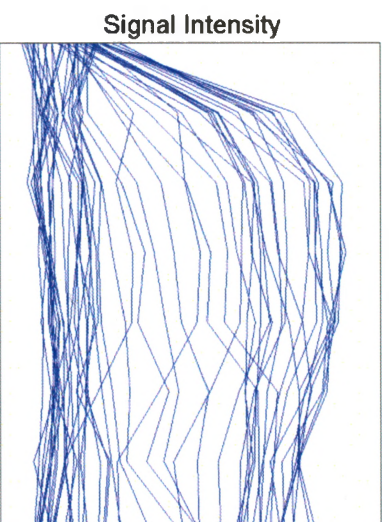
A



B



E



F

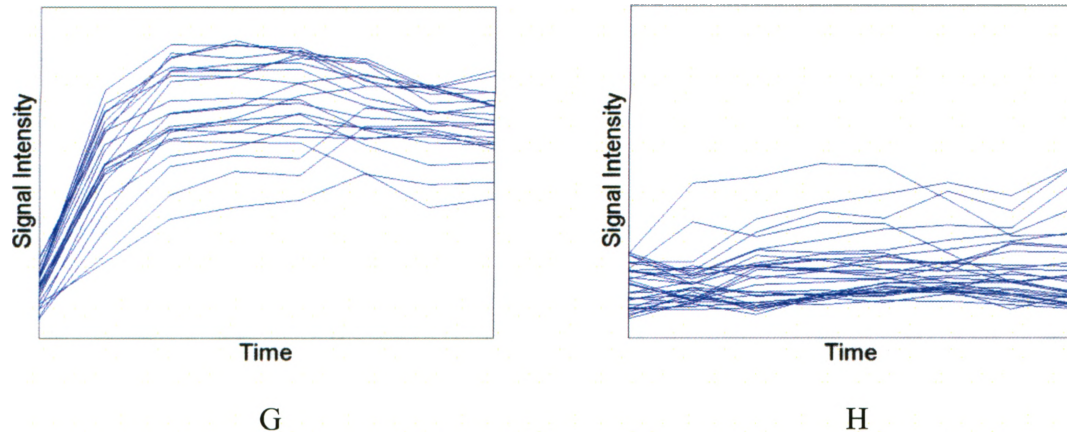


**Figure 1-2.** One example of lesion segmentation using the K-means clustering method from the data used for Chapter 2. Part A and B illustrate the lesions and neighbouring tissue regions within one slice of a pre-contrast and a first post-contrast image, respectively. The yellow rectangle is a 2D cut from the 3D box outlined by a radiologist. Part C illustrates a series of slices within the full 3D box on the first post-contrast image showing the areas with signal enhancement. Part D is a series of slices of the binary mask within the box after the classification by K-means clustering, in which white represents the lesion voxels, and black represents normal tissue. Part E is a three dimensional rendering of the segmented lesion. Part F, G and H are the signal curves for all the voxels within the box, the segmented lesion and the normal tissue region, respectively.

## 1.6.2 Curve Fitting with an Empirical Model

Curve fitting refers to a process of mathematically constructing a curve that best represents a series of data points. The shape of the curve is defined by a set of parameters and the values of the parameters are optimised using nonlinear optimization methods to provide the best fit to the data. Certain kinetic features of the curve can be calculated from the optimized parameter values.

Curve fitting methods can be used with empirical mathematical models as well as certain pharmacokinetic models that are described by analytic equations. Several previous studies (54-56) have employed empirical mathematical models for curve fitting of the signal values obtained at the acquisition time points following contrast injection. In one

report, Gal et al. (55) presented an evaluation of the goodness-of-fit for three pharmacokinetic models including those reported by Tofts and Kermode (57), Brix (58) and Hayton (59) as well as a simple three parameter empirical model. Voxel-by-voxel curve fitting was performed and the goodness of fit was evaluated for the whole breast and for enhanced regions outlined by the reporting radiologist. The mean values of correlation coefficients ( $R^2$ ) and mean square errors (MSE) were calculated by averaging these values over all voxels within the whole breast or enhanced region. With the empirical model, higher  $R^2$  values and lower MSE values were obtained as compared to the three pharmacokinetic models tested, indicating better fits with the empirical model. The three-parameter empirical model proposed by Gal et al. (55) is given as:

$$\Delta S(t) = a * t * e^{-\frac{t^c}{b}} ,$$

$$\Delta S(t) = S(t) - S_0 ,$$

where  $t$  is the time elapsed after the beginning of contrast agent administration;  $S(t)$  is signal intensity at time  $t$ ;  $S_0$  is signal intensity before contrast agent administration;  $a$ ,  $b$ ,  $c$  are free parameters which can vary voxel-by-voxel. In this thesis, voxel-by-voxel curve fitting using this mathematical empirical model proposed by Gal et al. (55) was implemented. The value of  $T_{\text{peak}}$  was calculated from the optimized values of the parameters using the following equation (55).

$$T_{\text{peak}} = (b/c)^{\frac{1}{c}} .$$

This model was chosen for the present thesis because of its simplicity and previously proven good performance in terms of goodness-of-fit for breast DCE-MRI data. Figure 1-3 illustrates the fitted curves for two voxels within a malignant tumor studied in Chapter 2.

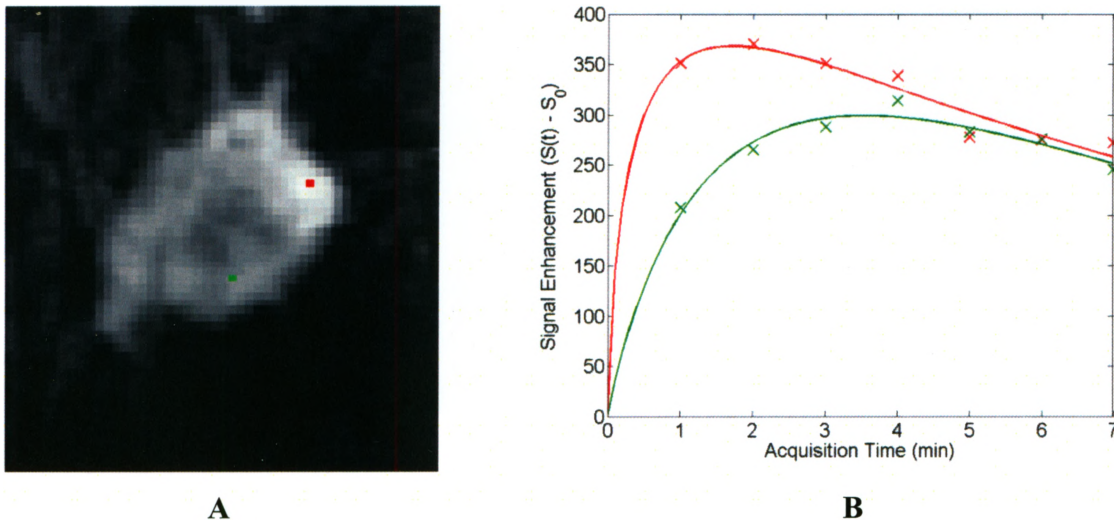


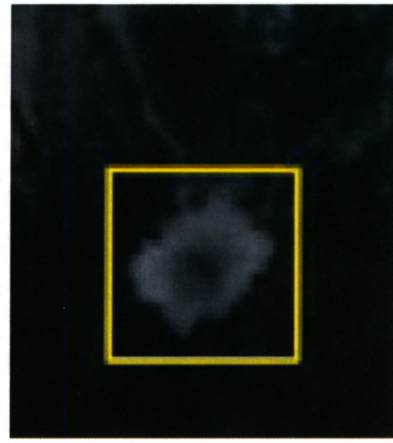
**Figure 1-3.** Curve fitting with the empirical model proposed by Gal et al. (55). Part A is one slice of the first post-contrast image showing an invasive ductal carcinoma. Within this lesion, the red and green points in Part A are two separate voxels, from which corresponding MR signals (after subtraction from pre-contrast) are demonstrated as red and green x's in part B, respectively. The solid lines in part B are the fitted curves using the empirical model by Gal et al. (55) for these two voxels. Note that  $T_{\text{peak}}$  values for these two voxels differ with a value of approximately 1.8 min for the red voxel and a value of approximately 3.5 min for the green voxel.

### 1.6.3 Histogram Analysis

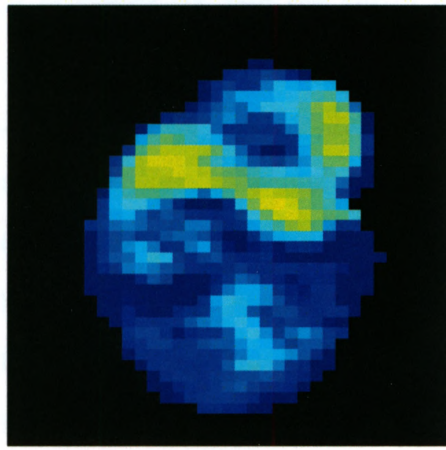
One simple way to characterize the intra-lesion  $T_{\text{peak}}$  distribution involves percentile values of the distribution. This is illustrated by the example histograms for one benign lesion (fibroadenoma) and one malignant lesion (invasive ductal carcinoma) illustrated in Figure 1-4. The difference between these distributions is apparent from the figure. *The histogram for the invasive ductal carcinoma lesion shows more voxels with shorter  $T_{\text{peak}}$  values compared to the fibroadenoma lesion.* To quantify these differences the percentile values (10<sup>th</sup>, 20<sup>th</sup> ... percentiles) can be determined. For example, the 10<sup>th</sup> percentile  $T_{\text{peak}}$  for the invasive ductal carcinoma (approximately 3 min) is approximately one min shorter than that of the fibroadenoma in this case.



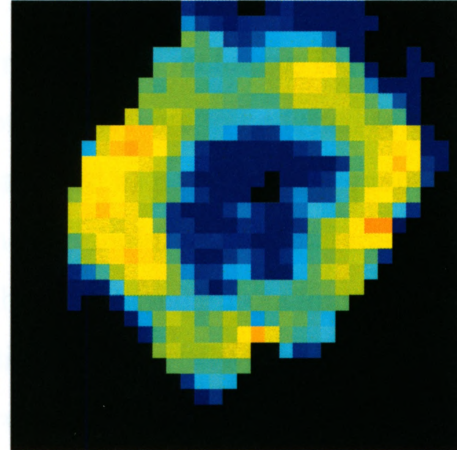
**A**



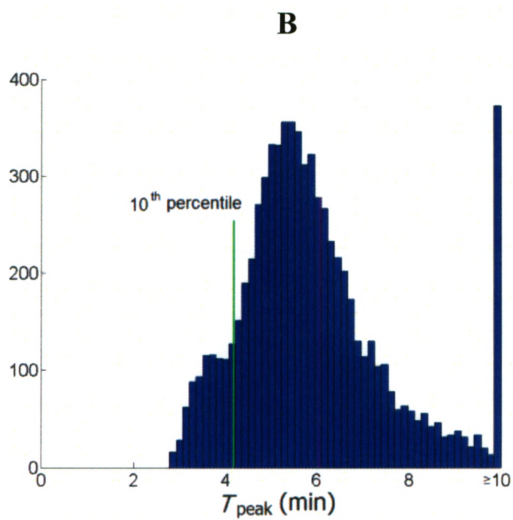
**D**



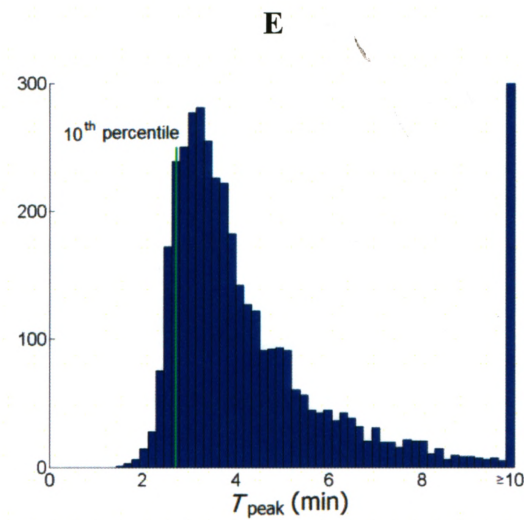
**B**  
 $T_{\text{peak}}$  (min)



**E**  
 $T_{\text{peak}}$  (min)



**C**



**F**

**Figure 1-4.**  $T_{\text{peak}}$  distribution demonstrates the intra-lesion heterogeneity of breast lesions. Part A shows a portion of one slice of the first post-contrast image from a patient with a fibroadenoma enclosed within a yellow box. Part B is the  $T_{\text{peak}}$  map

of this lesion at the same slice of Part A. The  $T_{\text{peak}}$  distribution for all lesion voxels within this benign lesion is shown in Part C. Part D shows a portion of one slice of the first post-contrast image from a patient with an invasive ductal carcinoma as enclosed within a yellow box. Corresponding  $T_{\text{peak}}$  map and  $T_{\text{peak}}$  distribution are shown in Part E and F, respectively.

## 1.7 Evaluation of Diagnostic Performance

The classification of lesion malignancy can be determined from biopsy examination (Chapter 2), and the result can be used as a reference (gold standard) for evaluating the diagnostic performance of other measures, including DCE-MRI measures of kinetics. For instance, if a threshold value of the measure to be tested (e.g., DCE-MRI measure) is chosen, then each lesion can be classified as positive (malignant) or negative (benign) based on whether or not it is above the threshold. These outcomes, based on the measure to be tested, can then be related to the gold standard outcomes, and each case can be designated as true positive, false positive, true negative or false negative. True positive represents the case which is determined as positive by both gold standard and the measure to be tested. True negative represents the case which is determined as negative by both gold standard and the measure. A false positive has occurred when the measure to be tested produces a positive outcome, but the gold standard indicates a negative outcome, and a false negative is the opposite case. These definitions are summarized in Table 1-1 below.

		Gold Standard	
		Positive ( $P$ )	Negative ( $N$ )
Measure	Positive	True Positive ( $TP$ )	False Positive ( $FP$ )
	Negative	False Negative ( $FN$ )	True Negative ( $TN$ )

**Table 1-1.** A  $2 \times 2$  contingency table for comparing the outcomes from a gold standard and a measure to be tested in binary classification.

The diagnostic sensitivity and specificity for the measure being tested, given a certain threshold value, is then defined as

$$\text{sensitivity} = \frac{TP}{P} ,$$
$$\text{specificity} = \frac{TN}{N} ,$$

where  $P$  and  $N$  are the number of positive and negative outcomes based on the gold standard.

The diagnostic performance of a measure for positive versus negative classification (e.g., malignant versus benign) can be evaluated using the receiver operating characteristic (ROC) curve (60, 61), which is a graphical plot of sensitivity versus 1-specificity. A ROC curve is created by determining the sensitivity and specificity as a function of threshold, across a range of threshold values that spans all of the data values, and then plotting sensitivity versus 1-specificity. The area under the ROC curve (AUC) can be used to evaluate the diagnostic performance of this measure, with higher AUC values corresponding to better diagnostic performance. Figure 1-5 illustrates hypothetical ROC curves for two different measures. Based on visual inspection measure 2 appears to have better diagnostic performance than measure 1 because its area under the curve (AUC) is larger. However, a formal comparison between two measures requires a specific statistical test (62).

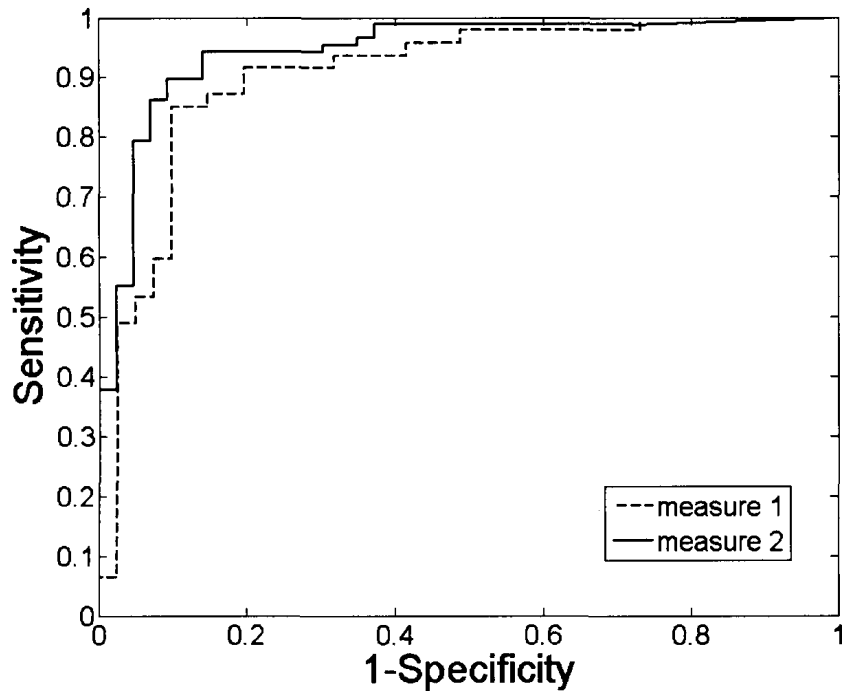


**Figure 1-5.** Hypothetical ROC curves for two measures. By changing the threshold value, sensitivity can be determined as a function of 1-specificity. The AUC value is the area under the ROC curve. In this example, measure 2 has a higher AUC value than measure 1.

## 1.8 Thesis Objectives

Although there has been a great deal of work on the development of quantitative kinetic feature analysis (both empirical and pharmacokinetic), much of this work has been based on the assessment of signals from manually derived regions of interest. Given the known heterogeneity of breast tumors, there is a need for further analyses aimed at obtaining kinetic information from entire lesions based on a voxel-by-voxel analysis. In addition, the literature on quantitative kinetic parameters contains very few reports that consider important differences between subgroups of malignant and benign tumors. As will be evident from chapter 2, the distinction between fibroadenomas and other benign tumors is important from the point of view of assessing diagnostic performance.

For this analysis I have chosen to focus on a single parameter known as the time-to-peak (section 1.5.1). As mentioned in section 1.5.1, a nice feature of the  $T_{\text{peak}}$  is that, at least in theory, it should be independent of imaging timing parameters since the maximal signal is expected to occur at the time at which the shortest  $T_1$  for a given voxel occurs. Also, despite the fact that the  $T_{\text{peak}}$  is a fundamental parameter in DCE, very little information exists in the literature about this parameter especially regarding the intra-lesion variation. To the best of my knowledge, most information presently in the literature is based on ROI measurements and the number of these studies is small.

This thesis involves the retrospective analysis of a large number of breast DCE magnetic resonance images from patients who received clinical MRI scans between Jan 2005 and Jan 2007. The retrospective analysis was considered as an appropriate starting point for our new research program in breast MRI. This research involves whole-tumor voxel-by-voxel analyses of measures related to the intra-lesion distribution of the  $T_{\text{peak}}$ . This included percentile values of the distribution as well as a measure to be referred to as the hot spot volume, which is the volume of lesion tissue in which the  $T_{\text{peak}}$  values for all voxels are less than a threshold value.

The specific objectives of this thesis are:

- 1) To assess the percentile values and hot spot volume as diagnostic indicators for the classification of (i) invasive malignant tumors from fibroadenomas (ii) invasive malignant tumors from non-fibroadenoma benign tumors (iii) DCIS lesions from fibroadenomas and (iv) DCIS lesions from non-fibroadenoma benign tumors.
- 2) To optimize these measures in terms of diagnostic performance.

## 1.9 Thesis Outline

In addressing the thesis objective, Chapter 2 deals with the investigation of the feasibility of applying measures ( $T_{\text{peak}}$  percentile and  $T_{\text{peak}}$  hot spot volume) sensitive to  $T_{\text{peak}}$  heterogeneity as indicators for malignancy in breast DCE-MRI. This chapter has been accepted for publication in *Academic Radiology* (Liu, F et al, 2011) and it contains an appendix that was included in the accepted manuscript. Chapter 3 provides a summary of the findings and a discussion of future work. Finally, two appendices are provided at the end of the thesis. Appendix I is one copy of the ethics approval by our Institutional Ethics Review Board. Appendix II contains my current curriculum vitae.

## 1.10 References

1. Canadian Cancer Statistics 2010, National Cancer Institute of Canada. Available at: [www.cancer.ca](http://www.cancer.ca). Accessed 2010.
2. Breast Cancer in Canada, Canadian Breast Cancer Foundation. Available at: [www.cbcbf.org/breastcancer/bc\\_whatbc\\_bc.asp](http://www.cbcbf.org/breastcancer/bc_whatbc_bc.asp). Accessed 2010.
3. Bevers TB. Primary Prevention of Breast Cancer, Screening for Early Detection of Breast Cancer, and Diagnostic Evaluation of Clinical and Mammographic Breast Abnormalities. In: Hunt KK ed. Breast Cancer 2nd edition. New York: Springer Science + Business Media; 2008.
4. Wadden N, Doyle GP. Breast cancer screening in Canada: a review. *Can Assoc Radiol J.* 2005; 56(5):271-5.
5. Elmore JG, Armstrong K, Lehman CD, Fletcher SW. Screening for breast cancer. *JAMA.* 2005; 293(10):1245-56.
6. Misra S, Solomon NL, Moffat FL, Koniaris LG. Screening criteria for breast cancer. *Adv Surg.* 2010; 44:87-100.
7. Giurescu ME, Hu T, Obembe O. Role of imaging in breast cancer detection. *AAOHN J.* 2010; 58(4):131-4.
8. Sinha S, Sinha U. Recent advances in breast MRI and MRS. *NMR Biomed.* 2009; 22(1):3-16.
9. Collins MJ, Hoffmeister J, Worrell SW. Computer-aided detection and diagnosis of breast cancer. *Semin Ultrasound CT MR.* 2006; 27(4):351-5.
10. Giger ML. Computerized analysis of images in the detection and diagnosis of breast cancer. *Semin Ultrasound CT MR.* 2004; 25(5):411-8.
11. Behrens S, Laue H, Althaus M, et al. Computer assistance for MR based diagnosis of breast cancer: present and future challenges. *Comput Med Imaging Graph.* 2007; 31(4-5):236-47.

12. Dupont WD, Page DL. Risk factors for breast cancer in women with proliferative breast disease. *N Engl J Med*. 1985; 312(3):146-51.
13. Mannello F, Tonti GA. Benign breast diseases: classification, diagnosis, and management. *Oncologist*. 2006; 11(10):1132-4; author reply 4.
14. Sklair-Levy M, Samuels TH, Catzavelos C, Hamilton P, Shumak R. Stromal fibrosis of the breast. *AJR Am J Roentgenol*. 2001; 177(3):573-7.
15. Folkman J, Klagsbrun M. Angiogenic factors. *Science*. 1987; 235(4787):442-7.
16. Frouge C, Guinebretiere JM, Contesso G, Di Paola R, Blery M. Correlation between contrast enhancement in dynamic magnetic resonance imaging of the breast and tumor angiogenesis. *Invest Radiol*. 1994; 29(12):1043-9.
17. Siedentopf F, Marten-Mittag B, Utz-Billing I, Schoenegg W, Kantenich H, Dinkel A. Experiences with a specific screening instrument to identify psychosocial support needs in breast cancer patients. *Eur J Obstet Gynecol Reprod Biol*. 2010; 148(2):166-71.
18. Carney PA, Miglioretti DL, Yankaskas BC, et al. Individual and combined effects of age, breast density, and hormone replacement therapy use on the accuracy of screening mammography. *Ann Intern Med*. 2003; 138(3):168-75.
19. Gordon PB. Ultrasound for breast cancer screening and staging. *Radiol Clin North Am*. 2002; 40(3):431-41.
20. Kolb TM, Lichy J, Newhouse JH. Occult cancer in women with dense breasts: detection with screening US--diagnostic yield and tumor characteristics. *Radiology*. 1998; 207(1):191-9.
21. Buchberger W, DeKoekoek-Doll P, Springer P, Obrist P, Dunser M. Incidental findings on sonography of the breast: clinical significance and diagnostic workup. *AJR Am J Roentgenol*. 1999; 173(4):921-7.
22. Berg WA, Blume JD, Cormack JB, et al. Combined screening with ultrasound and mammography vs mammography alone in women at elevated risk of breast cancer. *JAMA*. 2008; 299(18):2151-63.
23. Peters NH, Borel Rinkes IH, Zuithoff NP, Mali WP, Moons KG, Peeters PH. Meta-analysis of MR imaging in the diagnosis of breast lesions. *Radiology*. 2008; 246(1):116-24.
24. Wiener JI, Schilling KJ, Adami C, Obuchowski NA. Assessment of suspected breast cancer by MRI: a prospective clinical trial using a combined kinetic and morphologic analysis. *AJR Am J Roentgenol*. 2005; 184(3):878-86.
25. Deurloo EE, Peterse JL, Rutgers EJ, Besnard AP, Muller SH, Gilhuijs KG. Additional breast lesions in patients eligible for breast-conserving therapy by MRI: impact on preoperative management and potential benefit of computerised analysis. *Eur J Cancer*. 2005; 41(10):1393-401.
26. Kuroki Y, Nawano S, Hasebe T, et al. Efficacy of MR mammography (MRM) in providing preoperative locoregional information on breast cancer: correlation between MRM and histological findings. *Magn Reson Med Sci*. 2002; 1(2):73-80.
27. Tofts PS. Modeling tracer kinetics in dynamic Gd-DTPA MR imaging. *J Magn Reson Imaging*. 1997; 7(1):91-101.

28. Tofts PS, Brix G, Buckley DL, et al. Estimating kinetic parameters from dynamic contrast-enhanced T(1)-weighted MRI of a diffusable tracer: standardized quantities and symbols. *J Magn Reson Imaging*. 1999; 10(3):223-32.
29. Bains LJ, McGrath DM, Naish JH, et al. Tracer kinetic analysis of dynamic contrast-enhanced MRI and CT bladder cancer data: A preliminary comparison to assess the magnitude of water exchange effects. *Magn Reson Med*. 2010; 64(2):595-603.
30. Landis CS, Li X, Telang FW, et al. Determination of the MRI contrast agent concentration time course in vivo following bolus injection: effect of equilibrium transcytolemmal water exchange. *Magn Reson Med*. 2000; 44(4):563-74.
31. Judd RM, Reeder SB, May-Newman K. Effects of water exchange on the measurement of myocardial perfusion using paramagnetic contrast agents. *Magn Reson Med*. 1999; 41(2):334-42.
32. Buckley DL, Kershaw LE, Stanisz GJ. Cellular-interstitial water exchange and its effect on the determination of contrast agent concentration in vivo: dynamic contrast-enhanced MRI of human internal obturator muscle. *Magn Reson Med*. 2008; 60(5):1011-9.
33. Kaiser WA, Zeitler E. MR imaging of the breast: fast imaging sequences with and without Gd-DTPA. Preliminary observations. *Radiology*. 1989; 170(3 Pt 1):681-6.
34. Kuhl CK, Mielcareck P, Klaschik S, et al. Dynamic breast MR imaging: are signal intensity time course data useful for differential diagnosis of enhancing lesions? *Radiology*. 1999; 211(1):101-10.
35. Degani H, Gusis V, Weinstein D, Fields S, Strano S. Mapping pathophysiological features of breast tumors by MRI at high spatial resolution. *Nat Med*. 1997; 3(7):780-2.
36. Furman-Haran E, Grobgeld D, Margalit R, Degani H. Response of MCF7 human breast cancer to tamoxifen: evaluation by the three-time-point, contrast-enhanced magnetic resonance imaging method. *Clin Cancer Res*. 1998; 4(10):2299-304.
37. Furman-Haran E, Degani H. Parametric analysis of breast MRI. *J Comput Assist Tomogr*. 2002; 26(3):376-86.
38. Hauth EA, Stockamp C, Maderwald S, et al. Evaluation of the three-time-point method for diagnosis of breast lesions in contrast-enhanced MR mammography. *Clin Imaging*. 2006; 30(3):160-5.
39. Ikeda O, Yamashita Y, Morishita S, et al. Characterization of breast masses by dynamic enhanced MR imaging. A logistic regression analysis. *Acta Radiol*. 1999; 40(6):585-92.
40. Li KL, Henry RG, Wilmes LJ, et al. Kinetic assessment of breast tumors using high spatial resolution signal enhancement ratio (SER) imaging. *Magn Reson Med*. 2007; 58(3):572-81.
41. Szabo BK, Aspelin P, Wiberg MK, Bone B. Dynamic MR imaging of the breast. Analysis of kinetic and morphologic diagnostic criteria. *Acta Radiol*. 2003; 44(4):379-86.
42. Chen W, Giger ML, Bick U. A fuzzy c-means (FCM)-based approach for computerized segmentation of breast lesions in dynamic contrast-enhanced MR images. *Acad Radiol*. 2006; 13(1):63-72.

43. Chen W, Giger ML, Bick U, Newstead GM. Automatic identification and classification of characteristic kinetic curves of breast lesions on DCE-MRI. *Med Phys*. 2006; 33(8):2878-87.
44. Mussurakis S, Buckley DL, Coady AM, Turnbull LW, Horsman A. Observer variability in the interpretation of contrast enhanced MRI of the breast. *Br J Radiol*. 1996; 69(827):1009-16.
45. Mussurakis S, Buckley DL, Horsman A. Dynamic MR imaging of invasive breast cancer: correlation with tumour grade and other histological factors. *Br J Radiol*. 1997; 70(833):446-51.
46. Mussurakis S, Buckley DL, Horsman A. Dynamic MRI of invasive breast cancer: assessment of three region-of-interest analysis methods. *J Comput Assist Tomogr*. 1997; 21(3):431-8.
47. Liney GP, Gibbs P, Hayes C, Leach MO, Turnbull LW. Dynamic contrast-enhanced MRI in the differentiation of breast tumors: user-defined versus semi-automated region-of-interest analysis. *J Magn Reson Imaging*. 1999; 10(6):945-9.
48. Jackson A, O'Connor JP, Parker GJ, Jayson GC. Imaging tumor vascular heterogeneity and angiogenesis using dynamic contrast-enhanced magnetic resonance imaging. *Clin Cancer Res*. 2007; 13(12):3449-59.
49. Issa B, Buckley DL, Turnbull LW. Heterogeneity analysis of Gd-DTPA uptake: improvement in breast lesion differentiation. *J Comput Assist Tomogr*. 1999; 23(4):615-21.
50. Ertas G, Gulcur HO, Tunaci M. Improved lesion detection in MR mammography: three-dimensional segmentation, moving voxel sampling, and normalized maximum intensity-time ratio entropy. *Acad Radiol*. 2007; 14(2):151-61.
51. Karahaliou A, Vassiou K, Arikidis NS, Skiadopoulos S, Kanavou T, Costaridou L. Assessing heterogeneity of lesion enhancement kinetics in dynamic contrast-enhanced MRI for breast cancer diagnosis. *Br J Radiol*. 2010; 83(988):296-309.
52. Deurloo EE, Muller SH, Peterse JL, Besnard AP, Gilhuijs KG. Clinically and mammographically occult breast lesions on MR images: potential effect of computerized assessment on clinical reading. *Radiology*. 2005; 234(3):693-701.
53. Lee SH, Kim JH, Kim KG, Park JS, Park SJ, Moon WK. Optimal clustering of kinetic patterns on malignant breast lesions: comparison between K-means clustering and three-time-points method in dynamic contrast-enhanced MRI. *Conf Proc IEEE Eng Med Biol Soc*. 2007; 2007:2089-93.
54. Fan X, Medved M, Karczmar GS, et al. Diagnosis of suspicious breast lesions using an empirical mathematical model for dynamic contrast-enhanced MRI. *Magn Reson Imaging*. 2007; 25(5):593-603.
55. Gal Y, Mehnert A, Bradley A, McMahon K, Crozier S. An evaluation of four parametric models of contrast enhancement for dynamic magnetic resonance imaging of the breast. *Conf Proc IEEE Eng Med Biol Soc*. 2007; 2007:71-4.
56. Fan X, Medved M, River JN, et al. New model for analysis of dynamic contrast-enhanced MRI data distinguishes metastatic from nonmetastatic transplanted rodent prostate tumors. *Magn Reson Med*. 2004; 51(3):487-94.

57. Tofts PS, Kermode AG. Measurement of the blood-brain barrier permeability and leakage space using dynamic MR imaging. 1. Fundamental concepts. *Magn Reson Med.* 1991; 17(2):357-67.
58. Brix G, Semmler W, Port R, Schad LR, Layer G, Lorenz WJ. Pharmacokinetic parameters in CNS Gd-DTPA enhanced MR imaging. *J Comput Assist Tomogr.* 1991; 15(4):621-8.
59. Hayton P, Brady M, Tarassenko L, Moore N. Analysis of dynamic MR breast images using a model of contrast enhancement. *Med Image Anal.* 1997; 1(3):207-24.
60. Hanley JA, McNeil BJ. The meaning and use of the area under a receiver operating characteristic (ROC) curve. *Radiology.* 1982; 143(1):29-36.
61. Obuchowski NA. Receiver operating characteristic curves and their use in radiology. *Radiology.* 2003; 229(1):3-8.
62. Parker CB, DeLong ER. ROC methodology within a monitoring framework. *Stat Med.* 2003; 22(22):3473-88.

# Optimization of Time-to-peak Analysis for Differentiating Malignant and Benign Breast Lesions with Dynamic Contrast-Enhanced MRI

## 2.1 Introduction

Dynamic contrast-enhanced MRI (DCE-MRI) is utilized extensively for the diagnosis of breast lesions (1, 2). Clinical DCE-MRI analysis typically involves visual inspection of the time evolution of the signal enhancement and morphology of the enhanced region (3, 4). However, there is growing interest in the development and assessment of quantitative methods to provide objective and improved diagnostic indicators (5-13).

Quantitative analysis applied to the time evolution (kinetics) of breast DCE-MRI includes both empirical measures (7-9, 14) as well as pharmacokinetic models (15-18). While the latter have the advantage of providing physiological parameters, these models can be challenging to apply. There is ongoing research to deal with complex issues involved in their application, such as how to obtain accurate and robust arterial input functions (19) as well as the level of model complexity and time resolution required (20). Empirical measures on the other hand are much simpler to apply. They can be applied to images that have been acquired in clinical scans using imaging parameters (e.g., high spatial resolution, full breast coverage) that are preferred for radiological assessment but may not be ideal for pharmacokinetic model analysis.

One very simple empirical parameter that has shown promise as a diagnostic indicator is the time-to-peak ( $T_{\text{peak}}$ ) (7-9, 13, 14). This is the time duration from the contrast agent injection to the maximal MRI signal for a given voxel (8). A nice feature of the  $T_{\text{peak}}$  is that, at least in theory, it should be independent of imaging timing

parameters since the maximal signal is expected to occur at the time at which the shortest  $T_1$  for a given voxel occurs. Previous assessments of the  $T_{\text{peak}}$  in breast lesions have typically been obtained from signal enhancement curves averaged over a user-defined region of interest (ROI) (7-9, 14), although  $T_{\text{peak}}$  measurement from signal curves automatically selected using fuzzy c-means clustering has also been done (13). Given the known heterogeneity of breast lesions, in terms of other MRI derived parameters (21-24) and in terms of vascularity (25, 26), we propose that an assessment of the  $T_{\text{peak}}$  distribution based on voxel-by-voxel measurements should provide a means to further optimize the diagnostic performance and reproducibility of this measure.

The purpose of this work is to investigate the diagnostic performance of measures of the  $T_{\text{peak}}$  distribution for differentiating benign breast lesions (fibroadenomas and other non-fibroadenoma benign lesions) from malignant lesions (ductal carcinoma in situ and invasive carcinomas). In addition, we will consider the diagnostic performance of a measure to be referred to as the hot spot volume, which is the volume of lesion tissue in which the  $T_{\text{peak}}$  values for all voxels are less than a threshold value. The diagnostic performances of these measures are also compared to that obtained using  $T_{\text{peak}}$  values from manually drawn regions of interest. An investigation of the relation of hot spot volume to the lesion volume is also presented. Finally, we discuss the relation of the measured  $T_{\text{peak}}$  values to the pharmacokinetic parameter  $k_{\text{ep}}$  (rate constant for transport from interstitial space to plasma) in the context of the model presented by Tofts and Kermode (27).

## **2.2 Materials and Methods**

### **2.2.1 Patients and Lesions**

This study was a retrospective analysis of consecutive breast MRI scans obtained at our institute between January, 2005 and January, 2007. During this time period our institute offered breast MRI mainly in a diagnostic setting to further characterize findings seen on other modalities. This included further staging of proven breast cancer, exclusion

of multi focal/bilateral disease, the presence of multiple fibroadenomas and non conclusive findings seen on ultrasound.

Following approval from our Institutional Ethics Review Board, radiology reports and clinical charts for all patients (N = 221) who received a breast MRI exam including DCE between Jan. 1, 2005 and Jan. 1, 2007 were reviewed by a radiologist (A.K.). From this group, patients were included in this study only if the radiology report indicated positive DCE-MRI findings and the patient had received a breast biopsy or two years of clinical and imaging follow-up (N =109). From this group we excluded six patients for whom the areas of enhancement were likely physiological enhancement based on normal breast tissue on biopsy (N =3) or unexplained, probably benign areas of enhancement which remained stable on follow-up (N =3). Thus 103 patients remained in the study.

The histopathological types of the lesions studied are provided in Table 2-1. Histopathological type was determined from core biopsy results, except for seven of the fibroadenomas all of which had been described by the reporting radiologist as probably fibroadenomas based on features seen on breast ultrasound. In addition, the two year follow-up indicated that the patients with these fibroadenomas were free of breast cancer. Multiple fibroadenomas were present in three patients, including two patients each with two biopsy confirmed fibroadenomas and one patient without biopsy results. For the former patients only the biopsy confirmed fibroadenomas were analyzed and for the latter patient the largest fibroadenoma in each breast was analyzed. For much of the analysis, lesions were grouped into the following four categories: (i) invasive lesions (85 lesions from 72 patients) (ii) ductal carcinoma in situ (DCIS, 12 lesions from 12 patients) (iii) fibroadenomas (23 lesions from 17 patients) and (iv) benign lesions other than fibroadenomas (non-fibroadenoma benign lesion, 16 lesions from 15 patients), where some patients have lesions in more than one group. The mean ( $\pm$  SD) ages (years) of the patients in these four groups were  $53 \pm 10$ ,  $49 \pm 12$ ,  $45 \pm 11$  and  $47 \pm 11$ , respectively.

<b><i>Benign Lesions</i></b>	<b>39</b>
Fibroadenoma	23
Fibrosis	3
Fibrocystic Change	3
Intraductal Papilloma	2
Complex Papillary Lesion	3
Scar Tissue	2
Skin Lesion	1
Apocrine Metaplasia	1
Fat Necrosis	1
<b><i>Malignant Lesions</i></b>	<b>97</b>
Invasive Ductal Carcinoma (IDC)	76
Ductal Carcinoma in situ (DCIS)	12
Invasive Lobular Carcinoma (ILC)	5
Invasive Cancer with Mucinous Features	4
<b><i>All Lesions</i></b>	<b>136</b>

**Table 2-1** Histopathological diagnosis for the 136 breast lesions.

### 2.2.2 Image Acquisition

The DCE-MRI had been performed on a 1.5 T Siemens MRI system with a two-element breast coil (Siemens Avanto, Siemens, Erlangen, Germany). The 3D spoiled gradient echo sequence known as volume interpolated breath hold imaging (VIBE) was used with the following parameters:  $TR/TE = 4.5 \text{ ms}/1.2 \text{ ms}$ , flip angle =  $20^\circ$ , fat saturation with SPAIR, 6/8 partial Fourier in two directions. Parallel imaging with an acceleration factor of two was applied. The image matrix size was  $448 \times 318 \times 100$ , interpolated to  $512 \times 512 \times 160$  with a field of view ranging from  $300 \text{ mm} \times 300 \text{ mm} \times 176 \text{ mm}$  to  $350 \text{ mm} \times 350 \text{ mm} \times 176 \text{ mm}$ . Contrast agent administration involved manual injection of a 20 ml dose of gadopentetate dimeglumine (Gd-DTPA) (Magnevist, Bayer HealthCare Pharmaceuticals, USA) over 15 s to 20 s. The DCE acquisition consisted of 1 pre-contrast image and 7 post-contrast images with a temporal resolution of 1 min, with

the middle of first post-contrast image occurring 1 min after the start of Gd-DTPA administration.

### 2.2.3 Whole Lesion Image Analysis

#### *Lesion Segmentation*

First, a radiologist (A.K.) reviewed each patient's radiology report along with their magnetic resonance images viewed on a clinical work station, and then provided landmarks regarding lesion location, morphology and size. Following that, image analysis was performed in Matlab (Matlab R2009a, The MathWorks Inc., USA) using in-house scripts. Using a Matlab graphical user interface, a 3D rectangular box enclosing the lesion was positioned by a second radiologist (O.S.) on the first post-contrast image based on the provided landmarks. Voxels inside the box were classified into two clusters by K-means clustering (28) applied to the images obtained by subtracting the pre-contrast image from each post-contrast image. Euclidian distance was chosen as the criterion of similarity between each curve and the centroids in the classification. The cluster with the higher signal enhancement on the first post-contrast image averaged across all voxels was considered as the lesion. Groups of disconnected voxels less than 30 voxels (approximate 12 mm<sup>3</sup>) were eliminated in order to reduce the influence of the noise.

#### *Time-to-peak Analysis*

The signal evolution curve for each voxel was fit to the following three parameter model (29):

$$\Delta S(t) = a \cdot t \cdot e^{-\frac{t^c}{b}} ,$$

$$\Delta S(t) = S(t) - S_0 ,$$

where  $t$  is the time elapsed after the beginning of contrast agent administration;  $S(t)$  is signal intensity at time  $t$ ;  $S_0$  is signal intensity before contrast agent administration;  $a$ ,  $b$ ,  $c$  are free parameters which can vary from voxel to voxel. The Trust-Region algorithm was

applied for non-linear curve fitting. The  $T_{\text{peak}}$  of each curve was calculated using the following relationship (29):

$$T_{\text{peak}} = (b/c)^{\frac{1}{c}} .$$

For each lesion we determined the percentile values of the  $T_{\text{peak}}$  distribution over a range from the 10<sup>th</sup> to the 90<sup>th</sup> percentile (i.e.,  $p^{\text{th}}$  percentile where  $p$  varies from 10 to 90) as well as a quantity to be referred to as the “hot spot volume”, defined as the volume of tissue corresponding to voxels having  $T_{\text{peak}}$  values less than a certain threshold value. The dependence of the hot spot volume on threshold value was determined for all lesions using threshold values in the range from 1 min to 7 min. The hot spot volume was expressed as an absolute volume and as a fraction of the lesion volume (fractional volume).

#### **2.2.4 Region of Interest Image Analysis**

Manually drawn regions of interest (ROIs) were created in order to compare a ROI analysis with our whole lesion analysis. For each lesion, one region of interest (ROI) with at least three voxels (as recommended by the American College of Radiology) was drawn by a radiologist (A.K.) with specialization in breast imaging. For each ROI, the average signal intensity across all voxels in the ROI was determined for the pre-contrast image and each post-contrast image. The above mentioned fitting procedure was then applied to the resulting signal evolution curve and the  $T_{\text{peak}}$  was extracted.

#### **2.2.5 Receiver Operating Characteristic (ROC) Analysis**

Receiver operating characteristic (ROC) analysis was employed to assess the optimized  $T_{\text{peak}}$  percentile values, the optimized hot spot volumes and the ROI-based  $T_{\text{peak}}$  values as indicators for differentiating each of the two malignant lesion groups separately from each of the two benign lesion groups (i.e., fibroadenoma versus invasive lesions, fibroadenoma versus DCIS, non-fibroadenoma benign versus invasive and non-

fibroadenoma benign versus DCIS). The area under ROC curve (AUC), which is a measure of diagnostic performance, was determined (SPSS 17.0, SPSS Inc., USA) as a function of  $p$  for the percentile analysis and as a function of  $T_{\text{peak}}$  threshold for the hot spot volume analysis. To compare the diagnostic performance of different indicators, statistical comparisons between ROC curves were performed based on a previously described test (30) using MedCalc (MedCalc 11.3, MedCalc Software, Belgium). In addition, linear regression analysis was performed to investigate the relationship between hot spot volume and lesion volume for the four groups of lesions separately.

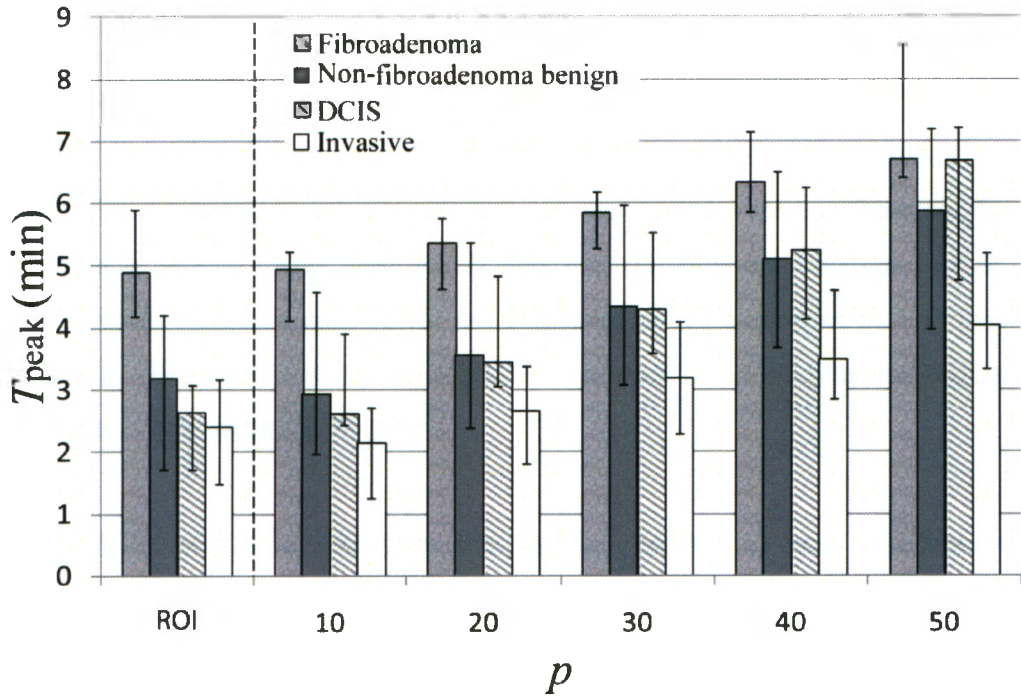
The ROC analyses were repeated using a subset of the invasive lesions for which the volumes of these lesions were matched to those of the benign lesions. (This analysis was not done with DCIS due to the small number of DCIS lesions.) First, the lesion volumes of the invasive group were compared with those of the fibroadenomas and then with those of the non-fibroadenoma benign lesions using a  $t$ -test. If the volume difference was significant, then the largest invasive lesion was excluded and the  $t$ -test repeated. This process was repeated until there was no significant difference ( $p > 0.05$ ) between the volumes of the lesions in each group. Finally, the ROC analysis for the 10<sup>th</sup> percentile and 50<sup>th</sup> percentile  $T_{\text{peak}}$  as well as for the ROI-based analysis were repeated with  $T_{\text{peak}}$  values less than 1 minute set to be exactly 1 minute and values greater than 7 minutes set to exactly 7 minutes.

## 2.3 Results

Figure 2-1a illustrates a bar graph of percentile values of the  $T_{\text{peak}}$  distributions as well as ROI-based  $T_{\text{peak}}$  values for lesions in each group. Each bar represents the median value for one group and the error bars indicate the interquartile range (i.e., 25<sup>th</sup> to 75<sup>th</sup> percentile). As displayed in this figure, malignant lesions (DCIS and invasive) tend to have lower percentile values than that of benign lesions (fibroadenoma and non-fibroadenoma benign lesion), especially at low  $p$  values. At higher  $p$  values than the 50<sup>th</sup>, the median values become larger than seven minutes (i.e., are obtained from extrapolation beyond the last post-contrast image with the fitting procedure). It was found that the 10<sup>th</sup>

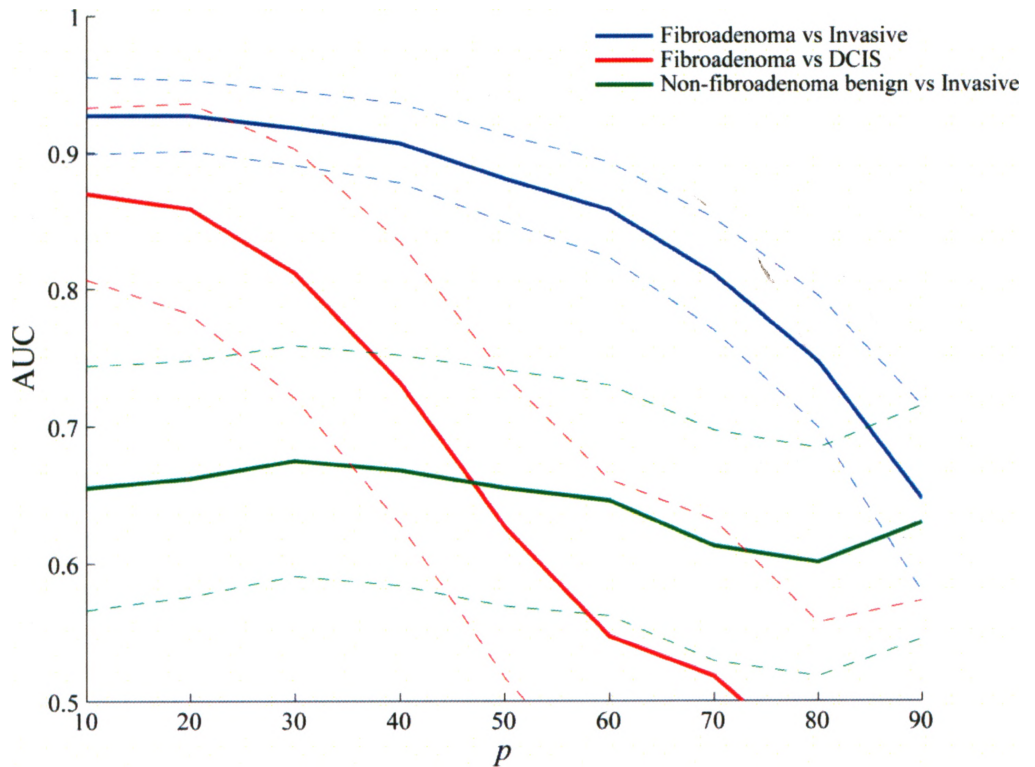
percentile  $T_{\text{peak}}$ , values for all lesions were less than seven minutes, but three non-fibroadenoma benign lesions and 13 invasive lesions had values less than one minute. However with increasing value of  $p$  more lesions had  $T_{\text{peak}}$  percentile values exceeding seven minutes, as one might expect from observing (Figure 2-1a) that with increasing value of  $p$  the top of the interquartile range approaches seven minutes. For the manual ROI-based analysis several lesions had values less than one minute (one fibroadenoma, three non-fibroadenoma benign lesions, two DCIS and six invasive lesions) or greater than seven minutes (five fibroadenoma, one non-fibroadenoma benign lesion, and four invasive lesions).

Figure 2-1b, which is a plot of AUC versus  $p$ , shows that the separation of fibroadenomas from invasive lesions and DCIS increases with decreasing  $p$ , especially for the latter separation. Although the AUC values corresponding to the separation of fibroadenomas from malignant lesions are reasonably high at low values of  $p$ , the AUC values for distinguishing non-fibroadenoma benign lesions from invasive lesions are low at any value of  $p$ . The AUC values for differentiating non-fibroadenoma benign lesions versus DCIS (not shown) are even lower than for non-fibroadenoma benign lesions versus invasive lesions.



$p$

**a**

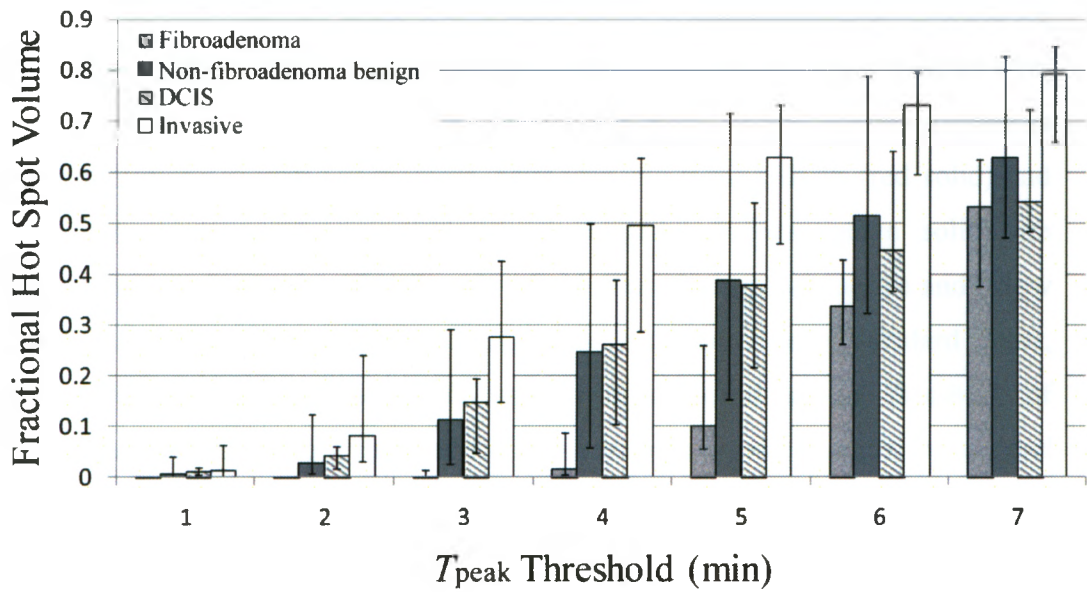


**b**

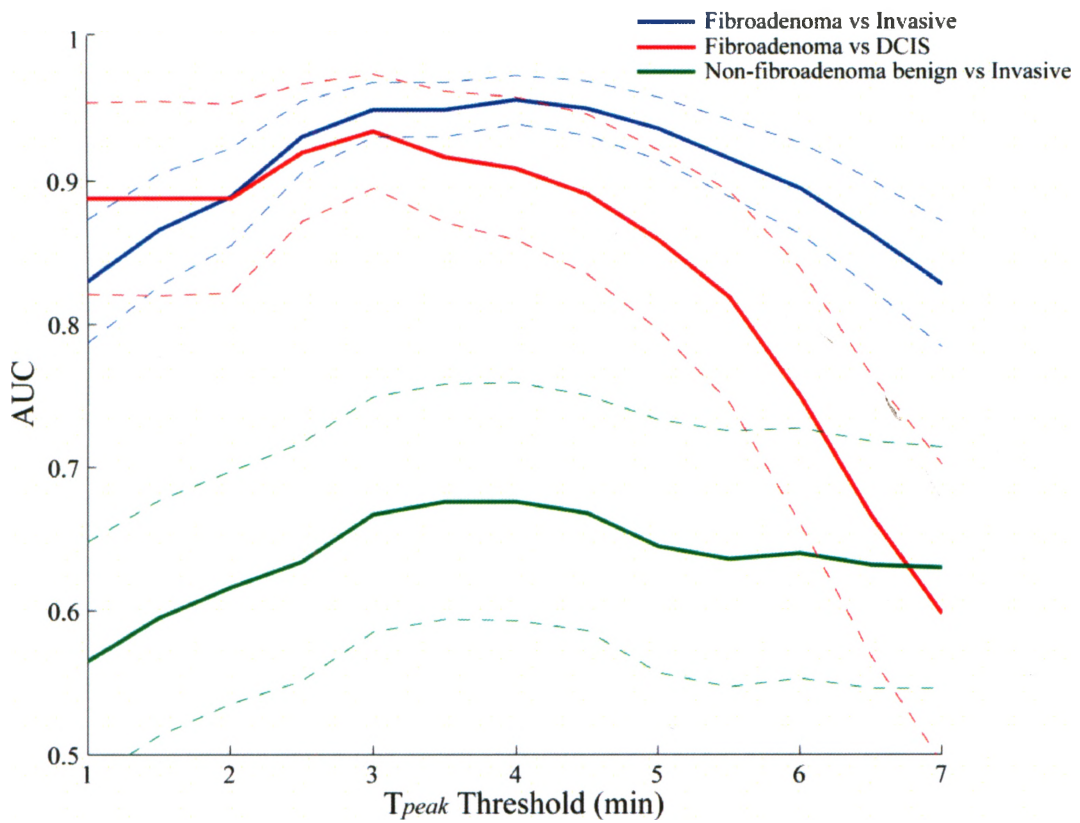
**Figure 2-1.** Median percentile  $T_{\text{peak}}$  values and ROI-based  $T_{\text{peak}}$  values (a) as well as AUC values corresponding to percentile  $T_{\text{peak}}$  values (b). In part (a) the median

and interquartile ranges (error bars) of the  $p^{\text{th}}$  percentile  $T_{\text{peak}}$  values ( $p = 10, 20 \dots 50$ ) and ROI-based  $T_{\text{peak}}$  values are shown for each of the four groups of lesions (fibroadenoma, non-fibroadenoma benign, DCIS and Invasive). The 10<sup>th</sup> percentile  $T_{\text{peak}}$  shows similar median values as does the ROI-based measure. In part (b), The AUC values for fibroadenoma versus invasive lesions (blue solid), fibroadenoma versus DCIS (red solid) and non-fibroadenoma benign lesions versus invasive lesions (green solid) are displayed as a function of  $p$ . The two dashed lines above and below each solid line represent the AUC plus and minus one standard error, respectively.

Figures 2-2a and 2-3a illustrate the median fractional and absolute hot spot volumes for the four groups of lesions obtained at several different  $T_{\text{peak}}$  thresholds. Fibroadenomas have the smallest fractional and absolute hot spot volumes at any  $T_{\text{peak}}$  threshold. Plots of AUC versus  $T_{\text{peak}}$  threshold (Figure 2-2b and 2-3b) indicate that the maximal AUC value for distinguishing fibroadenomas from invasive lesions and DCIS occurs at approximately three to four minutes. Although the AUC values for the separation of fibroadenomas from malignant lesions are high especially at thresholds of three to four minutes, AUC values for distinguishing non-fibroadenoma benign lesions from invasive lesions are low, at any threshold. The AUC values for distinguishing non-fibroadenoma benign lesions from DCIS (not shown) are also low ( $< 0.75$  and  $< 0.6$  for absolute and fractional hot spot volume, respectively). It should be noted that Figure 2-2a reflects similar information as that in Figure 2-1a ( $p^{\text{th}}$  percentile part), since the variable  $p$  is equivalent to fractional hot spot volume (expressed as a percent), and  $p^{\text{th}}$  percentile of the  $T_{\text{peak}}$  distribution is equivalent to the  $T_{\text{peak}}$  threshold value. However, the plots in part b of these figures differ, because Figure 2-1b illustrates an optimization with respect to  $p$  whereas Figure 2-2b illustrates an optimization with respect to  $T_{\text{peak}}$  threshold.



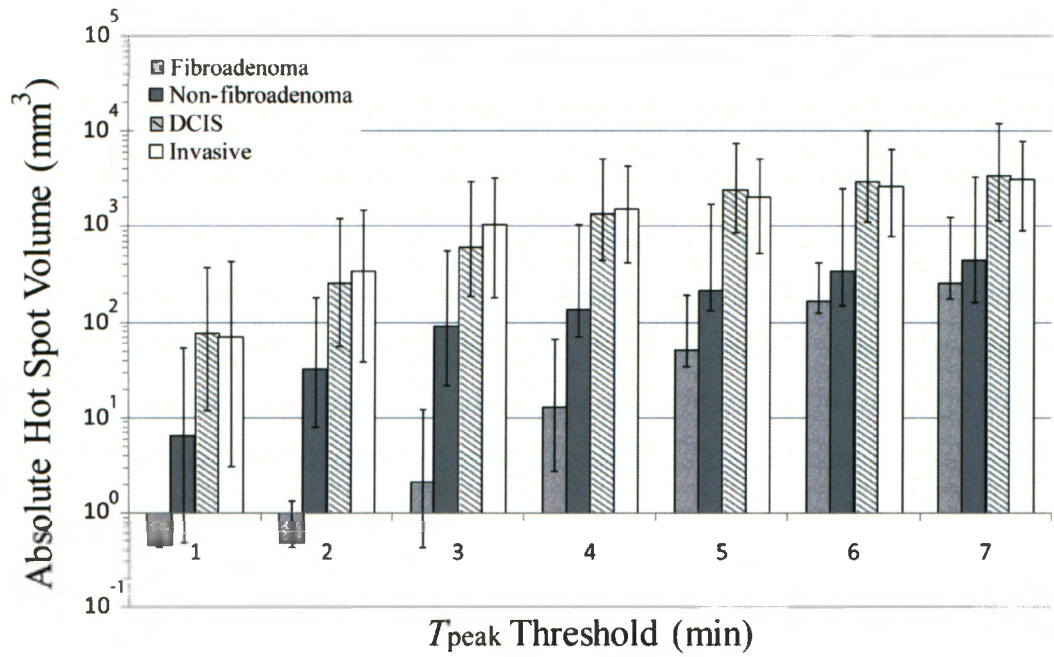
a



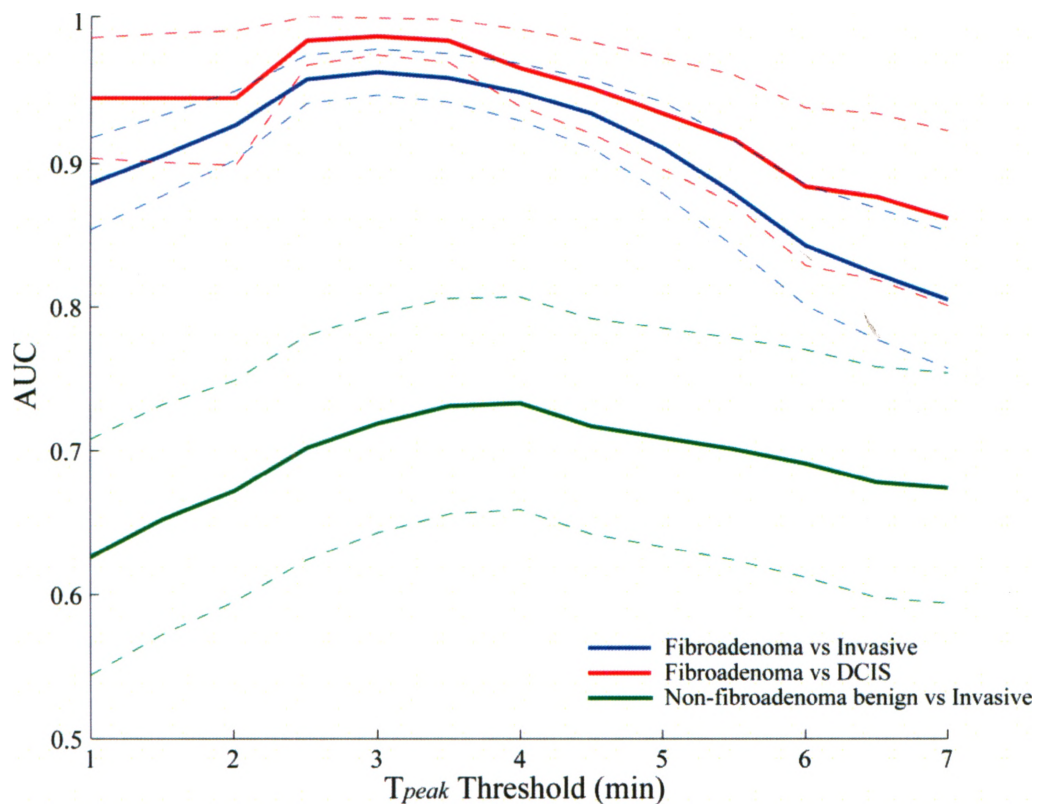
b

**Figure 2-2.** Median fractional hot spot volumes (a) and corresponding AUC values (b). The fractional hot spot volume is the fractional volume of tissue within the lesion having  $T_{peak}$  values less than a threshold value. In part (a) the

median and interquartile ranges (error bars) of the fractional hot spot volumes are shown for each of the four groups of lesions (fibroadenoma, non-fibroadenoma benign, DCIS and Invasive). In part (b), The AUC values for fibroadenoma versus invasive lesions (blue solid), fibroadenoma versus DCIS (red solid) and non-fibroadenoma benign lesions versus invasive lesions (green solid) are displayed as a function of the  $T_{\text{peak}}$  threshold. Two dashed lines above and below each solid line represent the AUC plus and minus one standard error, respectively. The maximal AUC values are achieved at the threshold of approximate three to four minutes for fibroadenoma versus invasive lesions and three minutes for fibroadenoma versus DCIS.



**a**



**b**

**Figure 2-3.** Median absolute hot spot volumes (a) and corresponding AUC values (b). The absolute hot spot volume is the volume of tissue within the lesion

having  $T_{\text{peak}}$  values less than a threshold value. In part (a) the median and interquartile ranges (error bars) of the fractional hot spot volumes are shown for each of the four groups of lesions (fibroadenoma, non-fibroadenoma benign, DCIS and Invasive). In part (b), The AUC values for fibroadenoma versus invasive lesions (blue solid), fibroadenoma versus DCIS (red solid) and non-fibroadenoma benign lesions versus invasive lesions (green solid) are displayed as a function of the  $T_{\text{peak}}$  threshold. Two dashed lines above and below each solid line represent the AUC plus and minus one standard error, respectively. The maximal AUC values are achieved at the threshold of approximate three to four minutes for fibroadenoma versus invasive lesions and for fibroadenoma versus DCIS.

The AUC values for ROI-based  $T_{\text{peak}}$ , 10<sup>th</sup> percentile  $T_{\text{peak}}$ , 50<sup>th</sup> percentile (median)  $T_{\text{peak}}$  as well as for the hot spot volumes with a  $T_{\text{peak}}$  threshold of 3 min are provided in Table 2-2. For distinguishing fibroadenomas from invasive lesions, the AUC value for the manual ROI-based  $T_{\text{peak}}$  is significantly lower than those for 10<sup>th</sup> percentile  $T_{\text{peak}}$  ( $p = 0.020$ ), fractional hot spot volume ( $p = 0.016$ ) and absolute hot spot volume ( $p = 0.024$ ). The AUC value for 50<sup>th</sup> percentile  $T_{\text{peak}}$  is significantly lower than those for fractional ( $p = 0.019$ ) and absolute hot spot volumes ( $p = 0.006$ ). For distinguishing fibroadenomas from DCIS, the AUC value for 10<sup>th</sup> percentile  $T_{\text{peak}}$  is significantly lower than that for the absolute hot spot volume ( $p = 0.039$ ), and the AUC value for the 50<sup>th</sup> percentile  $T_{\text{peak}}$  is significantly lower than the other values ( $p = 0.014$  for manual ROI-based  $T_{\text{peak}}$ ,  $p = 0.008$  for 10<sup>th</sup> percentile  $T_{\text{peak}}$ ,  $p = 0.001$  for fractional and absolute hot spot volumes). No other statistical differences were found for the rest of the comparisons, including those involving non-fibroadenoma benign lesions (bottom two rows of Table 2-2). AUC values determined with the constraint that percentile and ROI-based  $T_{\text{peak}}$  values less than one minute, or greater than seven minutes, were set equal to one minute or seven minutes, respectively (see Methods), showed only some small differences compared to those in Table 2-2. (For fibroadenoma vs. invasive, the AUC value for 50<sup>th</sup> percentile  $T_{\text{peak}}$  decreased by 0.01. For fibroadenoma vs. DCIS, AUC values for 10<sup>th</sup> and 50<sup>th</sup> percentile  $T_{\text{peak}}$  increased by 0.01 and 0.04, respectively. For comparisons with non-fibroadenoma benign lesions, values changed by 0.01 for ROI-based values and 0.03 or

less for percentiles.) ROC curves for distinguishing fibroadenomas from invasive lesions and from DCIS corresponding to ROI-based analysis and absolute hot spot volume at a threshold of 3 min are shown in Figure 2-4.

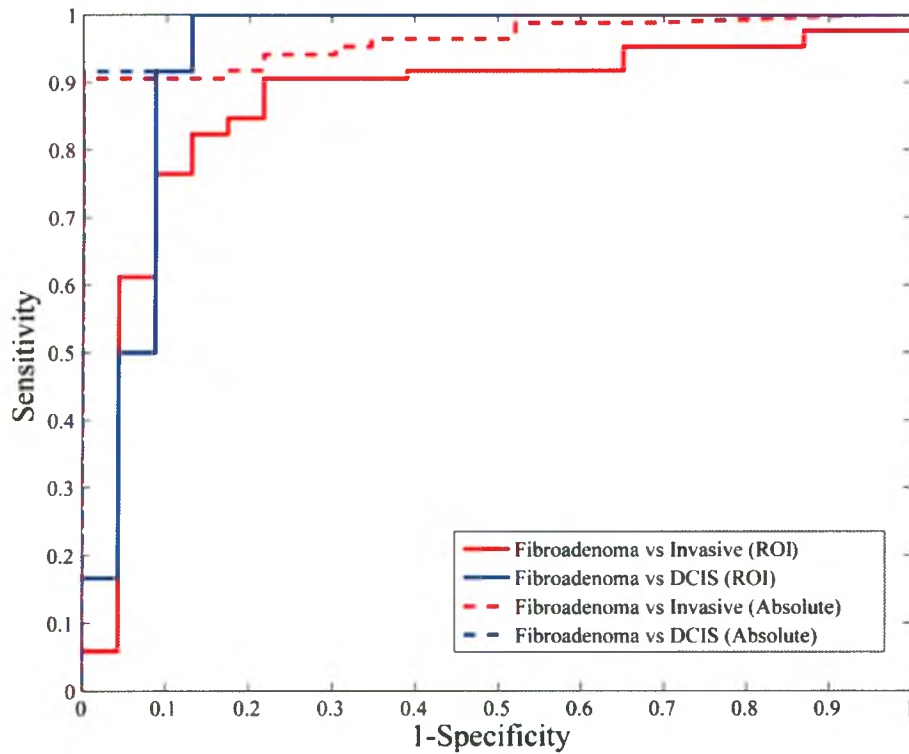


**Figure 2-4.** Receiver operating characteristic (ROC) curves for differentiating fibroadenoma versus invasive lesions and fibroadenoma versus DCIS using ROI-based analysis and absolute hot spot volume at a  $T_{\text{peak}}$  threshold of 3 min. The area under the curves (AUC values) for each test are  $0.87 \pm 0.05$ ,  $0.94 \pm 0.04$ ,  $0.96 \pm 0.02$  and  $0.99 \pm 0.01$ , respectively. Pairwise ROC curve comparison showed that for differentiating fibroadenoma from invasive lesions the absolute hot spot measure performed significantly better than the ROI-based measure. However, for differentiating fibroadenoma from DCIS no significant differences were found.

Comparison	AUC ± SE				
	Manual ROI	10 <sup>th</sup> percentile	50 <sup>th</sup> percentile	Fractional (3 min)	Absolute (3 min)
Fibroadenoma vs Invasive	0.87 ± 0.05 <sup>C</sup>	0.93 ± 0.03 <sup>A,B</sup>	0.88 ± 0.03 <sup>B,C</sup>	0.95 ± 0.02 <sup>A</sup>	0.96 ± 0.02 <sup>A</sup>
Fibroadenoma vs DCIS	0.94 ± 0.04 <sup>A,B</sup>	0.87 ± 0.06 <sup>B</sup>	0.63 ± 0.11 <sup>C</sup>	0.94 ± 0.04 <sup>A,B</sup>	0.99 ± 0.01 <sup>A</sup>
Non-fibroadenoma benign vs Invasive	0.58 ± 0.09 <sup>C</sup>	0.66 ± 0.09 <sup>C</sup>	0.66 ± 0.09 <sup>C</sup>	0.67 ± 0.08 <sup>C</sup>	0.72 ± 0.08 <sup>C</sup>
Non-fibroadenoma benign vs DCIS	0.63 ± 0.11 <sup>C</sup>	0.52 ± 0.11 <sup>C</sup>	0.41 ± 0.11 <sup>C</sup>	0.53 ± 0.11 <sup>C</sup>	0.71 ± 0.10 <sup>C</sup>

**Table 2-2** AUC values for 5 measures in differentiating 4 groups of breast lesions.

\* AUC: area under ROC curve; SE: standard error; DCIS: ductal carcinoma in situ.

† In the same row, measures with a different letter (<sup>A</sup>, <sup>B</sup>, <sup>C</sup>) are significantly different (ROC comparison test,  $p < 0.05$ ), and measures with the same letter are not significantly different (ROC comparison test,  $p \geq 0.05$ ).

The invasive lesions were found to have significantly larger volumes than those of the fibroadenomas but not significantly larger than those of the non-fibroadenoma benign lesions. In order to match the volumes of the invasive lesions to those of fibroadenomas (see Methods) it was necessary to eliminate the largest 23 invasive lesions. After this elimination, the AUC values for 10<sup>th</sup> and 50<sup>th</sup> percentile  $T_{\text{peak}}$  were slightly higher (by 0.01 and 0.02, respectively) than the corresponding values in Table 2-2. The AUC value for absolute hot spot volume was slightly lower (by 0.01) and that for fractional hot spot volume was unchanged. The standard errors were the same as those in Table 2-2.

A further investigation of the absolute hot spot volume at the optimal threshold (3 min) revealed a significant correlation (Table 2-3) between hot spot volume and lesion volume for the invasive lesions, the DCIS and the non-fibroadenoma benign lesions, but not for the fibroadenomas. The invasive lesions showed the largest rate of increase of hot spot volume with volume (i.e., slope of the regression line). These increases in hot spot volume with lesions volume are illustrated in Figure 2-5 as well as by the slopes of the linear regressions in Table 2-3. Note that although Figure 2-5 is a log-log plot, the parameters in Table 2-3 correspond to the relationship prior to log transformation. In

contrast to the changes in absolute hot spot volume with lesion volume, no significant correlation was found between fractional hot spot volume (at a threshold of 3 min) and lesion volume for any lesion group.

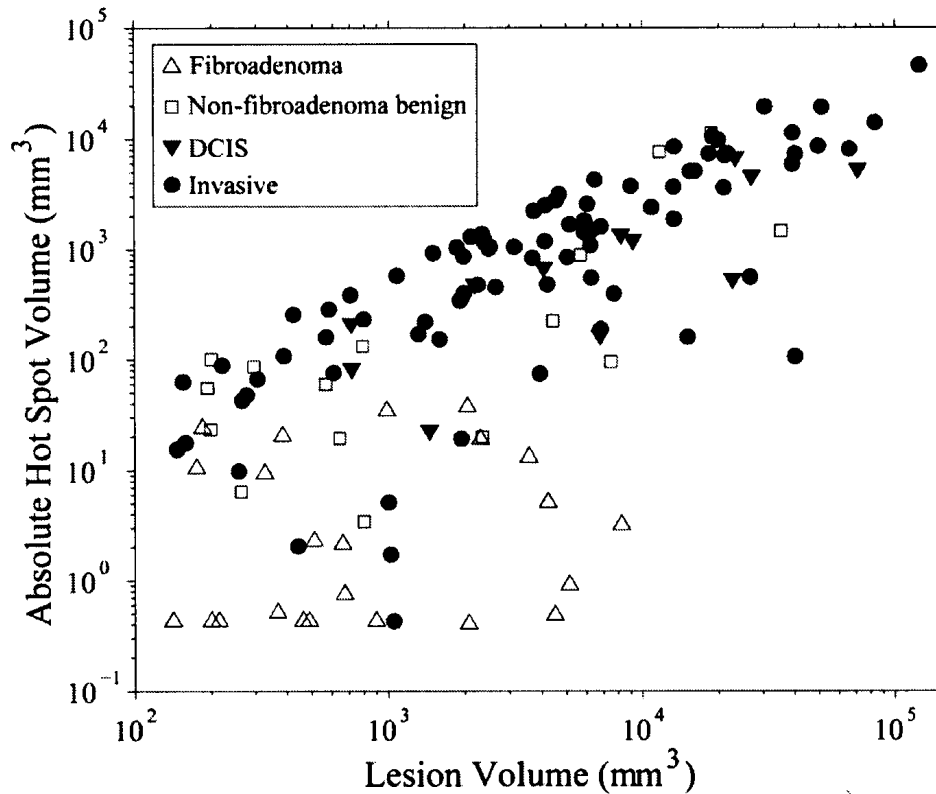


**Figure 2-5.** Relationship between absolute hot spot volume ( $T_{\text{peak}}$  threshold of 3 min) and lesion volume for fibroadenomas (empty up triangles), non-fibroadenoma benign lesions (empty squares), DCIS (filled down triangles) and invasive lesions (filled circles). Note the log scale on both axes. Fibroadenomas tend to have smaller absolute hot spot volumes than those of malignant lesions. The relationship of absolute hot spot volume to lesion volume is similar for non-fibroadenoma benign lesions and malignant lesions. The non-fibroadenoma benign lesions, DCIS and invasive lesions show a significant linear correlation between absolute hot spot volume and lesion volume (Table 2-3).

	Coefficient		F Statistics		
	Slope	Intercept ( $\times 10^2 \text{ mm}^3$ )	$R^2$	F value	p value
Non-fibroadenoma benign	$0.17 \pm 0.08$	$4 \pm 9$	0.26	4.9	0.04
DCIS	$0.09 \pm 0.03$	$5 \pm 7$	0.53	11	0.007
Invasive	$0.27 \pm 0.02$	$0.5 \pm 4$	0.74	243	<0.001

**Table 2-3** Linear regression analysis for absolute hot spot volume at a threshold of 3 min versus lesion volume.

The absolute hot spot volumes ( $T_{\text{peak}}$  threshold of 3 min) are shown for all lesions grouped according to histopathological type in Figure 2-6. This plot confirms that fibroadenomas appear to be the most easily distinguished from malignant lesions. The absolute hot spot volumes for histopathological types of non-fibroadenoma benign lesions show greater overlap with malignant lesions.

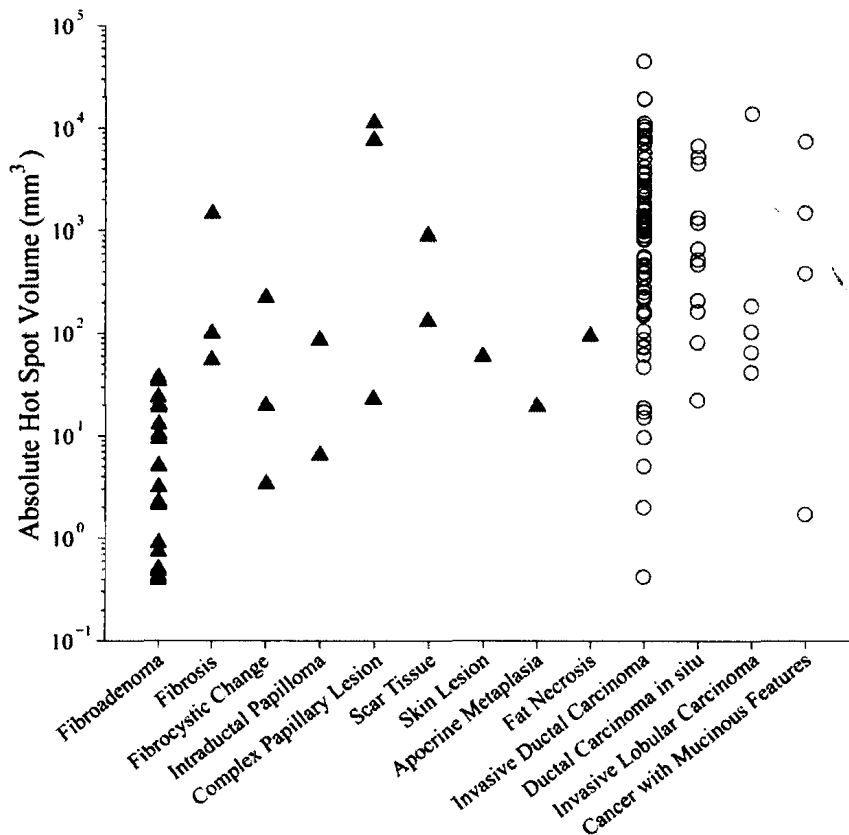


**Figure 2-6.** Absolute hot spot volumes at a  $T_{\text{peak}}$  threshold of 3 min for lesions within each histopathological type. Each triangle (benign) or circle (malignant)

represents one lesion. Fibroadenomas appear to be more easily distinguished from malignant lesions as compared to other benign lesions.

## 2.4 Discussion

In this study we investigated several measures based on the time-to-peak as indicators for distinguishing (i) fibroadenomas from invasive lesions, (ii) fibroadenomas from DCIS (iii) non-fibroadenoma benign lesions from invasive lesions and (iv) non-fibroadenoma benign lesions from DCIS. Based on the area under the ROC curves (Table 2-2), most of these indicators performed very well for distinguishing fibroadenomas from both types of malignant lesions, but poorly for distinguishing non-fibroadenoma benign lesions from the malignant lesions. This observation exemplifies the challenge in comparing diagnostic performance values obtained in different studies which differ in terms of the distribution (relative number) of lesions of each histopathological type. Several previous studies have qualitatively demonstrated that various non-fibroadenoma benign lesions can exhibit similar signal kinetics as malignant lesions (31-34). Perhaps a combined approach using  $T_{\text{peak}}$  analysis, i.e., 10<sup>th</sup> percentile of  $T_{\text{peak}}$  distribution or hot spot volume at threshold of 3 min, and the methods (10-12) of characterizing lesion morphology and texture would then provide better diagnostic performance for differentiating non-fibroadenoma benign lesions from malignant lesions. Unfortunately, because of the small sample sizes of non-fibroadenoma benign lesions in our study, it was not possible to determine the extent to which histological sub-types within the non-fibroadenoma benign group of lesions could be discriminated from malignant lesions.

Although previous studies have utilized the  $T_{\text{peak}}$  as a diagnostic indicator, they have usually involved manual ROI selection followed by the extraction of the  $T_{\text{peak}}$  of the mean signal across voxels within the ROI (7-9, 14). In our study, the 10<sup>th</sup> percentile  $T_{\text{peak}}$  and hot spot volumes did provide significantly better discrimination of fibroadenomas from invasive lesions than the  $T_{\text{peak}}$  values based on manually drawn ROIs. However, for discriminating fibroadenomas from DCIS there was no significant difference between the manual ROI analysis and the 10<sup>th</sup> percentile  $T_{\text{peak}}$  and hot spot volumes, although this

comparison may have been limited by the small number ( $N = 12$ ) of DCIS lesions. It should be noted that manual ROI selection is subject to inter- and intra-observer variation (35-38), which may lead to varying diagnostic performance and lower reproducibility, compared to more automated procedures.

Our results suggest that the overlap between fibroadenomas and malignant lesions tends to be minimized close to the lower end of the  $T_{\text{peak}}$  distribution, especially for the fibroadenoma versus DCIS comparison. Thus the diagnostic performance of employing the  $T_{\text{peak}}$  as a diagnostic indicator depends on the way in which the distribution of  $T_{\text{peak}}$  values is sampled, likely due to the wide range of  $T_{\text{peak}}$  values existing within each lesion (i.e., lesion heterogeneity). Previous reports have utilized statistical quantities sensitive to heterogeneity of various DCE-MRI measures as indicators in the diagnosis of breast lesions (21, 23, 24, 26). For example, in an early study involving measurement of the pharmacokinetic parameter  $K^{\text{trans}}$ , measures of the width of the  $K^{\text{trans}}$  distribution provided higher diagnostic performance for differentiating breast cancer from benign lesions compared with the mean of  $K^{\text{trans}}$  (21). In a more recent study, using the normalized maximum intensity-time ratio (nMITR), the entropy of the nMITR distribution provided the best indicator for quantitative diagnosis (23). Recently, the heterogeneity of breast lesions was investigated using several features of the grey level co-occurrence matrices (GLCM) applied to empirical parameter maps (24). Analysis reflecting lesion heterogeneity have also been applied to the diagnosis of other lesions and to assess changes following treatment (26).

In addition to the percentile values of the  $T_{\text{peak}}$  distribution, we also quantified the absolute and fractional hot spot volumes (volume of tissue corresponding to voxels having  $T_{\text{peak}}$  values less than a threshold), and assessed these measures as diagnostic indicators. For both fractional and absolute hot spot volumes, threshold  $T_{\text{peak}}$  value of approximately three to four minutes appeared optimal. It is reasonable to expect that the absolute hot spot volume would be a stronger indicator because it is “weighted” by the lesion volume which tends to be larger in malignant versus benign lesions. Although the AUC values (Table 2-2) obtained from absolute hot spot volume were slightly larger than

that of the fractional hot spot volume, the differences were not statistically significant in this data set. One advantage of utilizing the absolute hot spot volume rather than the fractional hot spot volume is that the former measure may be less sensitive to lesion segmentation methods than the latter. The non hot spot voxels included in the “lesion region” should not influence the absolute hot spot volume as long as all hot spots are determined.

An interesting finding of this study is that the absolute hot spot volume ( $T_{\text{peak}}$  threshold = 3 min) for invasive lesions, DCIS and non-fibroadenoma benign lesions correlated to lesion volume, with the strongest correlation for the invasive lesions (Table 2-3 and Figure 2-5). No correlation was found for fibroadenomas. The observed decrease in absolute hot spot volume with decreasing volume (Figure 2-5) suggests that the separation of malignant lesions from fibroadenomas based on absolute hot spot volume may be weaker for the smallest lesions compared to the larger ones. Finally, the finding that no significant correlation existed between the fractional hot spot volume and lesion volume also suggests that the hot spot volume scales with lesion volume.

In our analysis the  $T_{\text{peak}}$  values for each voxel (and for the ROI-based signals) were determined with the aid of curve fitting using an empirical model. Although  $T_{\text{peak}}$  values could have been determined from the raw signal values, curve fitting likely provides better precision and continuity than determination from raw signal data especially considering limited signal to noise ratio of single voxel data. The accuracy of the  $T_{\text{peak}}$  values depends on how well the empirical model describes the signals. The results of a previous assessment of this model for breast DCE signal analysis found higher  $R^2$  values and lower mean square errors than for three pharmacokinetic models tested (29).

In our analysis  $T_{\text{peak}}$  values determined by the curve fitting procedure were for some curves outside of the one minute to seven minute time span over which the images were acquired. The values obtained for the hot spot volumes were not dependent on the particular  $T_{\text{peak}}$  values obtained by the extrapolation, but only depended on the number of voxels with  $T_{\text{peak}}$  values less than the threshold. Thus, the hot spot analysis was not

influenced by the extrapolation. Although the percentile and ROI-based  $T_{\text{peak}}$  values used in the ROC analysis included some values outside of the one minute to seven minute time window, the ROC analyses corresponding to AUC values in Table 2-2 were also repeated with  $T_{\text{peak}}$  values less than one minute set to be exactly one minute and values greater than seven minutes set to exactly seven minutes. These are similar to constraints used previously (14) and represent the limits of  $T_{\text{peak}}$  measurements in analysis without curve fitting (7-9, 13). For the separation of fibroadenomas from invasive lesions the AUC for 10<sup>th</sup> percentile  $T_{\text{peak}}$  obtained with constraints was identical to that obtained without, presumably because the only unconstrained values outside of the one to seven minute window were the values for invasive lesions and these were less than one minute (i.e., they were all less than the lowest fibroadenoma value in either case). For other AUC values in Table 2-2, the difference between AUC values obtained with and without the constraints, were small (see Results).

A limitation of this study is that patients were given the same dose of contrast agent independent of patient weight. This may have introduced additional variation into the  $T_{\text{peak}}$  data. However, it can be shown (Appendix A) that in the context of the pharmacokinetic model presented by Tofts and Kermode (27), the  $T_{\text{peak}}$  is independent of dose. The extent to which this independence of dose holds in actual patient data is not known. Thus it is possible that if this analysis had been applied to patient data obtained using the same dose per body weight for each patient, unwanted variation might have been reduced and diagnostic performance improved.

Although this paper focused on the application of the  $T_{\text{peak}}$  distribution to provide empirical diagnostic indicators, it is nevertheless worthwhile to consider how the  $T_{\text{peak}}$  values can be related to a pharmacokinetic parameter  $k_{\text{ep}}$ , the rate constant for transporting contrast agent from interstitial space to plasma, in the context of the pharmacokinetic model presented by Tofts and Kermode (27). Within this model, the maximum signal intensity should occur at the point in time at which the contrast agent concentration in the tissue is maximal. Using this assumption, the  $T_{\text{peak}}$  depends only on  $k_{\text{ep}}$  and the parameters describing the arterial input function (see Appendix A). Figure 2-7

illustrates a plot of  $k_{ep}$  versus  $T_{peak}$  using the arterial input function originally measured by Weinmann (39) and modeled by Tofts and Kermode (27). Using Figure 2-7, we find that the optimal  $T_{peak}$  threshold (3 min) for hot spot volume measurement corresponds to a  $k_{ep}$  value of  $1 \text{ min}^{-1}$ . Also using this figure, the  $k_{ep}$  values corresponding to our median (50<sup>th</sup> percentile)  $T_{peak}$  values can be compared to  $k_{ep}$  from a previous study (22) which applied the Tofts and Kermode model directly and assumed the same arterial input function. This previous study (22) obtained  $k_{ep}$  values of  $0.44 \text{ min}^{-1}$  for fibroadenoma,  $0.32 \text{ min}^{-1}$  for benign stromal and epithelial tissue overgrowth and  $0.55 \text{ min}^{-1}$  for DCIS,  $0.85 \text{ min}^{-1}$  for IDC, where the values quoted were obtained by taking the median value of the  $k_{ep}$  distribution for each lesion and then taking the mean of these median values over the lesion group. Based on Figure 2-1a and 2-7, our 50<sup>th</sup> percentile (median) values over the  $T_{peak}$  distribution correspond to  $k_{ep}$  values of  $0.32 \text{ min}^{-1}$  for fibroadenoma,  $0.38 \text{ min}^{-1}$  for non-fibroadenoma benign lesions,  $0.33 \text{ min}^{-1}$  for DCIS and  $0.64 \text{ min}^{-1}$  for invasive lesions, which is a reasonable correspondence considering differences in lesion segmentation.

In summary, the percentile values of the  $T_{peak}$  distribution and hot spot volumes were investigated and optimized as indicators for breast lesion malignancy using the area under the receiver operating characteristic as a performance measure. In the percentile analysis, the lower edge (i.e., 10<sup>th</sup> percentile) of the  $T_{peak}$  distribution provided the highest diagnostic performance for differentiating fibroadenomas from malignant lesions, particularly DCIS. For the hot spot volume analysis, the highest diagnostic performance was obtained with a threshold of approximately three to four minutes for fibroadenoma versus malignant lesions. However, non-fibroadenoma benign lesions were found to be much more difficult to distinguish from malignant lesions, based on  $T_{peak}$  percentile, hot spot volume method or ROI-based  $T_{peak}$  values. Quantitative analysis of the  $T_{peak}$  distribution can be optimized for diagnostic performance providing indicators that are sensitive to  $T_{peak}$  heterogeneity over the lesion.

## 2.5 Appendix

The concentration of contrast agent  $C(t)$  in tissue at time  $t$  is given by the two compartment Tofts and Kermode model as(27):

$$C(t) = D \cdot K^{trans} \cdot \sum_{i=1}^2 a_i \cdot \frac{e^{-k_{ep} \cdot t} - e^{-m_i \cdot t}}{m_i - k_{ep}} ,$$

where  $D$  is the dose of contrast agent (Gd-DTPA) normalized by body weight (mmol/kg),  $K^{trans}$  is the endothelial transfer constant for transporting contrast agent from plasma to interstitial space,  $k_{ep}$  represents the rate constant for transport from interstitial space to plasma. Also  $a_i$  and  $m_i$  are the amplitudes and rate constants describing the two exponential components of the arterial input function.

Since the MRI signal increases monotonically with decreasing  $T_1$ , the maximal signal is expected to occur at the time at which the shortest  $T_1$  occurs. This is the time at which the highest tissue concentration of Gd-DTPA for a given voxel occurs. Also, the  $T_{peak}$  is the time at which the first derivative of  $C(t)$  is equal to 0. Using the equation above this condition is expressed by the following:

$$0 = \sum_{i=1}^2 a_i \cdot \frac{m_i \cdot e^{-m_i \cdot T_{peak}} - k_{ep} \cdot e^{-k_{ep} \cdot T_{peak}}}{m_i - k_{ep}} .$$

Thus the  $T_{peak}$  only depends on  $k_{ep}$  and the parameters of the arterial input function ( $a_1$ ,  $a_2$ ,  $m_1$  and  $m_2$ ). Numerical simulation by solving the equation above provides the relationship between  $T_{peak}$  and  $k_{ep}$  as shown in Figure 2-7, assuming the values for  $a_1$ ,  $a_2$ ,  $m_1$  and  $m_2$  are 3.99 kg/L, 4.78 kg/L, 0.144 min<sup>-1</sup> and 0.0111 min<sup>-1</sup>, respectively as provided in reference (27).

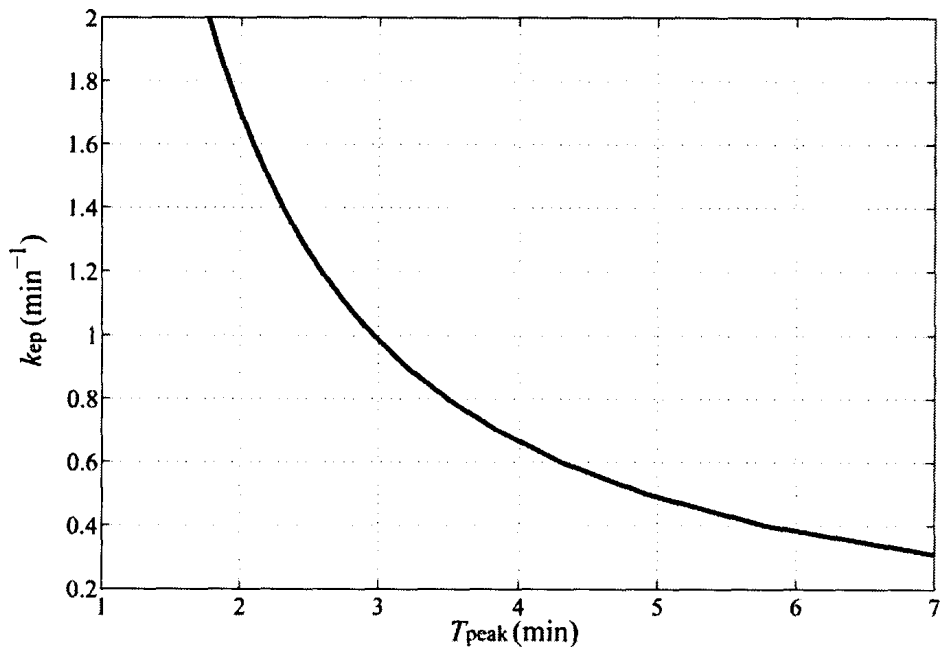


**Figure 2-7.** Relationship of  $T_{\text{peak}}$  and  $k_{\text{ep}}$  obtained by numerical simulation. The simulation utilized the pharmacokinetic model presented by Tofts and Kermode (27) and assumed the arterial input function measured by Weinmann (39).

## 2.6 References

1. Turnbull LW. Dynamic contrast-enhanced MRI in the diagnosis and management of breast cancer. *NMR Biomed.* 2009; 22(1):28-39.
2. Peters NH, Borel Rinkes IH, Zuithoff NP, Mali WP, Moons KG, Peeters PH. Meta-analysis of MR imaging in the diagnosis of breast lesions. *Radiology.* 2008; 246(1):116-24.
3. Ikeda DM, Hylton NM, Kinkel K, et al. Development, standardization, and testing of a lexicon for reporting contrast-enhanced breast magnetic resonance imaging studies. *J Magn Reson Imaging.* 2001; 13(6):889-95.
4. Schnall MD, Blume J, Bluemke DA, et al. Diagnostic architectural and dynamic features at breast MR imaging: multicenter study. *Radiology.* 2006; 238(1):42-53.
5. Kelcz F, Santyr GE, Cron GO, Mongin SJ. Application of a quantitative model to differentiate benign from malignant breast lesions detected by dynamic, gadolinium-enhanced MRI. *J Magn Reson Imaging.* 1996; 6(5):743-52.
6. Buckley DL, Kerslake RW, Blackband SJ, Horsman A. Quantitative analysis of multi-slice Gd-DTPA enhanced dynamic MR images using an automated simplex minimization procedure. *Magn Reson Med.* 1994; 32(5):646-51.

7. Ikeda O, Yamashita Y, Morishita S, et al. Characterization of breast masses by dynamic enhanced MR imaging. A logistic regression analysis. *Acta Radiol.* 1999; 40(6):585-92.
8. Szabo BK, Aspelin P, Wiberg MK, Bone B. Dynamic MR imaging of the breast. Analysis of kinetic and morphologic diagnostic criteria. *Acta Radiol.* 2003; 44(4):379-86.
9. Szabo BK, Wiberg MK, Bone B, Aspelin P. Application of artificial neural networks to the analysis of dynamic MR imaging features of the breast. *Eur Radiol.* 2004; 14(7):1217-25.
10. Liney GP, Sreenivas M, Gibbs P, Garcia-Alvarez R, Turnbull LW. Breast lesion analysis of shape technique: semiautomated vs. manual morphological description. *J Magn Reson Imaging.* 2006; 23(4):493-8.
11. Ertas G, Gulcur HO, Tunaci M. Normalized maximum intensity time ratio maps and morphological descriptors for assessment of malignancy in MR mammography. *Med Phys.* 2008; 35(5):1893-900.
12. Nie K, Chen JH, Yu HJ, Chu Y, Nalcioglu O, Su MY. Quantitative analysis of lesion morphology and texture features for diagnostic prediction in breast MRI. *Acad Radiol.* 2008; 15(12):1513-25.
13. Chen W, Giger ML, Bick U, Newstead GM. Automatic identification and classification of characteristic kinetic curves of breast lesions on DCE-MRI. *Med Phys.* 2006; 33(8):2878-87.
14. Jansen SA, Fan X, Karczmar GS, et al. DCEMRI of breast lesions: is kinetic analysis equally effective for both mass and nonmass-like enhancement? *Med Phys.* 2008; 35(7):3102-9.
15. Larsson HB, Stubgaard M, Frederiksen JL, Jensen M, Henriksen O, Paulson OB. Quantitation of blood-brain barrier defect by magnetic resonance imaging and gadolinium-DTPA in patients with multiple sclerosis and brain tumors. *Magn Reson Med.* 1990; 16(1):117-31.
16. Brix G, Semmler W, Port R, Schad LR, Layer G, Lorenz WJ. Pharmacokinetic parameters in CNS Gd-DTPA enhanced MR imaging. *J Comput Assist Tomogr.* 1991; 15(4):621-8.
17. Tofts PS, Berkowitz B, Schnall MD. Quantitative analysis of dynamic Gd-DTPA enhancement in breast tumors using a permeability model. *Magn Reson Med.* 1995; 33(4):564-8.
18. Hayton P, Brady M, Tarassenko L, Moore N. Analysis of dynamic MR breast images using a model of contrast enhancement. *Med Image Anal.* 1997; 1(3):207-24.
19. Port RE, Knopp MV, Brix G. Dynamic contrast-enhanced MRI using Gd-DTPA: interindividual variability of the arterial input function and consequences for the assessment of kinetics in tumors. *Magn Reson Med.* 2001; 45(6):1030-8.
20. Behrens S, Laue H, Althaus M, et al. Computer assistance for MR based diagnosis of breast cancer: present and future challenges. *Comput Med Imaging Graph.* 2007; 31(4-5):236-47.
21. Issa B, Buckley DL, Turnbull LW. Heterogeneity analysis of Gd-DTPA uptake: improvement in breast lesion differentiation. *J Comput Assist Tomogr.* 1999; 23(4):615-21.

22. Furman-Haran E, Schechtman E, Kelcz F, Kirshenbaum K, Degani H. Magnetic resonance imaging reveals functional diversity of the vasculature in benign and malignant breast lesions. *Cancer*. 2005; 104(4):708-18.
23. Ertas G, Gulcur HO, Tunaci M. Improved lesion detection in MR mammography: three-dimensional segmentation, moving voxel sampling, and normalized maximum intensity-time ratio entropy. *Acad Radiol*. 2007; 14(2):151-61.
24. Karahaliou A, Vassiou K, Arikidis NS, Skiadopoulos S, Kanavou T, Costaridou L. Assessing heterogeneity of lesion enhancement kinetics in dynamic contrast-enhanced MRI for breast cancer diagnosis. *Br J Radiol*. 2010; 83(988):296-309.
25. Carmeliet P, Jain RK. Angiogenesis in cancer and other diseases. *Nature*. 2000; 407(6801):249-57.
26. Jackson A, O'Connor JP, Parker GJ, Jayson GC. Imaging tumor vascular heterogeneity and angiogenesis using dynamic contrast-enhanced magnetic resonance imaging. *Clin Cancer Res*. 2007; 13(12):3449-59.
27. Tofts PS, Kermode AG. Measurement of the blood-brain barrier permeability and leakage space using dynamic MR imaging. 1. Fundamental concepts. *Magn Reson Med*. 1991; 17(2):357-67.
28. Lee SH, Kim JH, Kim KG, Park JS, Park SJ, Moon WK. Optimal clustering of kinetic patterns on malignant breast lesions: comparison between K-means clustering and three-time-points method in dynamic contrast-enhanced MRI. *Conf Proc IEEE Eng Med Biol Soc*. 2007; 2007:2089-93.
29. Gal Y, Mehnert A, Bradley A, McMahon K, Crozier S. An evaluation of four parametric models of contrast enhancement for dynamic magnetic resonance imaging of the breast. *Conf Proc IEEE Eng Med Biol Soc*. 2007; 2007:71-4.
30. Parker CB, DeLong ER. ROC methodology within a monitoring framework. *Stat Med*. 2003; 22(22):3473-88.
31. Chen JH, Liu H, Baek HM, Nalcioğlu O, Su MY. Magnetic resonance imaging features of fibrocystic change of the breast. *Magn Reson Imaging*. 2008; 26(9):1207-14.
32. Daly CP, Jaeger B, Sill DS. Variable appearances of fat necrosis on breast MRI. *AJR Am J Roentgenol*. 2008; 191(5):1374-80.
33. Iglesias A, Arias M, Santiago P, Rodriguez M, Manas J, Saborido C. Benign breast lesions that simulate malignancy: magnetic resonance imaging with radiologic-pathologic correlation. *Curr Probl Diagn Radiol*. 2007; 36(2):66-82.
34. Kurz KD, Roy S, Modder U, Skaane P, Saleh A. Typical atypical findings on dynamic MRI of the breast. *Eur J Radiol*. 2010; 76(2):195-210.
35. Mussurakis S, Buckley DL, Coady AM, Turnbull LW, Horsman A. Observer variability in the interpretation of contrast enhanced MRI of the breast. *Br J Radiol*. 1996; 69(827):1009-16.
36. Mussurakis S, Buckley DL, Horsman A. Dynamic MR imaging of invasive breast cancer: correlation with tumour grade and other histological factors. *Br J Radiol*. 1997; 70(833):446-51.
37. Mussurakis S, Buckley DL, Horsman A. Dynamic MRI of invasive breast cancer: assessment of three region-of-interest analysis methods. *J Comput Assist Tomogr*. 1997; 21(3):431-8.

38. Liney GP, Gibbs P, Hayes C, Leach MO, Turnbull LW. Dynamic contrast-enhanced MRI in the differentiation of breast tumors: user-defined versus semi-automated region-of-interest analysis. *J Magn Reson Imaging*. 1999; 10(6):945-9.
39. Weinmann HJ, Laniado M, Mutzel W. Pharmacokinetics of GdDTPA/dimeglumine after intravenous injection into healthy volunteers. *Physiol Chem Phys Med NMR*. 1984; 16(2):167-72.

## Summary and Future Work

### 3.1 Summary of Findings

The  $T_{\text{peak}}$  is a fundamental empirical parameter describing the kinetics of the DCE-MRI signal. Although a few previous studies have reported on measures of the  $T_{\text{peak}}$  in malignant and benign lesions, this thesis has gone well beyond these previous studies by (i) providing measures of the intra-lesion distribution of this parameter (ii) optimizing the diagnostic performance of the distribution measures and (iii) assessing this performance specifically for classification involving subgroups of malignant and benign tumors.

This thesis provides novel methods for investigating the intra-lesion heterogeneity of  $T_{\text{peak}}$  values with voxel-by-voxel based analysis. To the best of our knowledge, most of the analyses for quantitative kinetic features including  $T_{\text{peak}}$  were performed based on signals from manually drawn ROIs, in which a single  $T_{\text{peak}}$  was extracted from the average curve across this ROI. In Chapter 2, the analysis of the  $T_{\text{peak}}$  distribution based on a voxel-by-voxel  $T_{\text{peak}}$  extraction across the whole lesion indicated that the smallest overlap between benign and malignant breast lesions occurs at the lower end of the distribution (e.g. 10<sup>th</sup> percentile). The diagnostic performance of employing kinetic features, at least for  $T_{\text{peak}}$ , was demonstrated to be largely dependent of the way in which the distribution of the feature values is sampled. In addition, measures referred to as  $T_{\text{peak}}$  hot spot volumes including absolute and fractional hot spot volume were also investigated. The  $T_{\text{peak}}$  hot spot volume differed between benign and malignant breast lesions with the characteristics that malignant lesions generally have larger hot spot volume than that of benign ones.

In most previous DCE-MRI analyses, benign lesions were mixtures of various histopathological types including fibroadenomas, fibrocystic changes, etc. Although it has been known that differences in kinetic features may exist between breast lesion sub-

types, very few quantitative DCE-MRI studies involving manual or automatic methods have been done that considered the influence of lesion sub-type on diagnostic performance. In this thesis, benign lesions were divided into a fibroadenoma group and non-fibroadenoma benign lesion group, and malignant lesions were divided into invasive lesion group and DCIS group. All the  $T_{\text{peak}}$  measures were analyzed separately for each of the lesion sub-types (e.g., fibroadenoma vs. invasive, non-fibroadenoma benign lesion vs. DCIS, etc.). My results help to quantitatively demonstrate the challenges for differentiating non-fibroadenoma benign lesions from malignant lesions, while fibroadenomas are much more easily separated from malignant lesions. This result is important from a research perspective because the relative proportion of fibroadenoma and non-fibroadenoma benign lesions varies greatly across different reported studies and hence may be an important factor contributing to differences in diagnostic performance between these studies. While the greater diagnostic challenge associated with non-fibroadenoma benign lesions, compared to fibroadenomas is known to radiologists, reported studies on the development of quantitative automated or semi-automated methods have mostly not considered these subgroups. In most of these quantitative analyses, benign lesions have been a mixture of fibroadenomas and non-fibroadenoma benign lesions, and in some cases the majority of benign lesions have been fibroadenomas. Thus, this work may provide further motivation for researchers developing automated/semi-automated methods to demonstrate performance on both fibroadenomas and non-fibroadenoma benign lesions.

The investigation of the relationship of an empirical kinetic feature ( $T_{\text{peak}}$ ) and a pharmacokinetic parameter  $k_{\text{ep}}$  in the Tofts and Kermode model is an interesting aspect of the discussion presented in Chapter 2. A monotonic theoretical relationship was established by computer simulation showing that  $k_{\text{ep}}$  decreases with increasing  $T_{\text{peak}}$ . The  $T_{\text{peak}}$  values obtained in Chapter 2 after conversion to  $k_{\text{ep}}$  values provided a reasonable correspondence to the results from one previous published study (1) considering the differences in lesion segmentation. One study previously performed by Li et al. (2) also provided a means of associating an empirical kinetic feature, known as the signal enhancement ratio (*SER*) (see section 1.5.1) with  $k_{\text{ep}}$ . However, given the fact that *SER*

values are sensitive to the time points chosen, the method of mapping  $T_{\text{peak}}$  to  $k_{\text{ep}}$  should be more advantageous.

## 3.2 Future Work

Chapter 2 demonstrates the analysis of measures related to the distribution of  $T_{\text{peak}}$  across whole lesions. This method can be easily translated to analyze other empirical kinetic features and possibly pharmacokinetic parameters including  $K_{\text{trans}}$  and  $k_{\text{ep}}$  (when accurate arterial input functions and native  $T_1$  maps are available or properly estimated). In particular, the percentile values and hot spot volumes can be determined for other kinetic features. As mentioned above, given the heterogeneous nature of breast lesions, the diagnostic performance of kinetic features largely depends on the location within the lesions from where the features were extracted and how they were sampled.

One important extension of this work would involve assessing the spatial distribution of  $T_{\text{peak}}$  values and of the hot spot regions, within breast lesions. In this thesis, the analysis of intra-lesion heterogeneity of  $T_{\text{peak}}$  has mostly concentrated on the  $T_{\text{peak}}$  value distribution and measures relevant to tissue volume, but the spatial distribution of voxels with regard to the  $T_{\text{peak}}$  values was not considered. In particular, we do not know if the shorter  $T_{\text{peak}}$  (i.e.  $T_{\text{peak}}$  hot spot) regions tend to be contiguous or separated and possibly scattered within the lesion. Also, we do not know if the  $T_{\text{peak}}$  hot spot regions tend to be located centrally or peripherally within the lesions. Measures of this spatial location may provide further diagnostic indicators. Several previous studies have demonstrated that peripheral enhancement of breast lesions is an important indicator for lesion malignancy (3, 4). An investigation of the spatial distribution of the  $T_{\text{peak}}$  (e.g.  $T_{\text{peak}}$  map) may be helpful for characterizing intra-lesion structure and texture.

Future work may also involve assessing the influence of DCE-MRI spatial resolution on the  $T_{\text{peak}}$  analysis. It is expected that high spatial resolution should be valuable for heterogeneity-based analyses, since spatial variation is much better represented with high spatial resolution compared to low resolution images, especially for

analyzing small lesions. Previous studies (5-7) have demonstrated the critical role of high resolution for obtaining good diagnostic performance in differentiating benign versus malignant breast lesions. The images analyzed in this work had voxel sizes (prior to interpolation) of approximately  $1 \text{ mm} \times 1 \text{ mm} \times 2 \text{ mm}$ . However, in present clinical scans at our institute, one of the post-contrast images is acquired with even higher spatial resolution which has the voxel size approximately 3 times smaller than images used in this work. Future work could involve assessing the  $T_{\text{peak}}$  analysis with these higher resolution images.

Finally, a further investigation of the relationship between  $T_{\text{peak}}$  and  $k_{\text{ep}}$  would be interesting. This relationship as presented in Chapter 2 was based on a population averaged arterial input function. In future, the influence of the assumed arterial input function on this relationship could be assessed. The verification of this relationship could be performed using human breast MR data with accurate measures of the AIF and native  $T_1$  relaxation times.

### 3.3 Conclusions

In addressing the objective of the thesis, it has been shown that quantitative analysis of the  $T_{\text{peak}}$  distribution including percentile analysis and  $T_{\text{peak}}$  hot spot volume analysis can be optimized for diagnostic performance providing indicators that are sensitive to  $T_{\text{peak}}$  heterogeneity over the breast lesion. In the  $T_{\text{peak}}$  percentile analysis, the lower edge (i.e., 10<sup>th</sup> percentile) of the  $T_{\text{peak}}$  distribution provided the highest diagnostic performance for differentiating fibroadenomas from malignant lesions, particularly DCIS. For the  $T_{\text{peak}}$  hot spot volume analysis, a threshold of approximate three to four min was obtained for best separating fibroadenoma from malignant lesions. However, non-fibroadenoma benign lesions were generally found to be much more difficult to distinguish from malignant lesions.

### **3.4 References**

1. Furman-Haran E, Schechtman E, Kelcz F, Kirshenbaum K, Degani H. Magnetic resonance imaging reveals functional diversity of the vasculature in benign and malignant breast lesions. *Cancer*. 2005; 104(4):708-18.
2. Li KL, Henry RG, Wilmes LJ, et al. Kinetic assessment of breast tumors using high spatial resolution signal enhancement ratio (SER) imaging. *Magn Reson Med*. 2007; 58(3):572-81.
3. Nunes LW, Schnall MD, Orel SG, et al. Breast MR imaging: interpretation model. *Radiology*. 1997; 202(3):833-41.
4. Szabo BK, Aspelin P, Wiberg MK, Bone B. Dynamic MR imaging of the breast. Analysis of kinetic and morphologic diagnostic criteria. *Acta Radiol*. 2003; 44(4):379-86.
5. Degani H, Gushki V, Weinstein D, Fields S, Strano S. Mapping pathophysiological features of breast tumors by MRI at high spatial resolution. *Nat Med*. 1997; 3(7):780-2.
6. Furman-Haran E, Grobgedl D, Kelcz F, Degani H. Critical role of spatial resolution in dynamic contrast-enhanced breast MRI. *J Magn Reson Imaging*. 2001; 13(6):862-7.
7. Kelcz F, Furman-Haran E, Grobgedl D, Degani H. Clinical testing of high-spatial-resolution parametric contrast-enhanced MR imaging of the breast. *AJR Am J Roentgenol*. 2002; 179(6):1485-92.